Remote Sensing of Environment 114 (2010) 738–760

Contents lists available at ScienceDirect

Remote Sensing of Environment

journal homepage: www.elsevier.com/locate/rse

Assessing the coupling between surface albedo derived from MODIS and the fraction of diffuse skylight over spatially-characterized landscapes

Miguel O. Román [a,b,*], Crystal B. Schaaf [a], Philip Lewis [c], Feng Gao [b,d], Gail P. Anderson [e,f], Jeffrey L. Privette [g], Alan H. Strahler [a], Curtis E. Woodcock [a], Michael Barnsley [h]

[a] Department of Geography and Environment, Boston University, Boston, MA, USA
[b] Hydrospheric and Biospheric Sciences Laboratory, NASA Goddard Space Flight Center, Greenbelt, MD, USA
[c] Department of Geography, University College London, London, UK
[d] Earth Resources Technology, Inc., Annapolis Junction, MD, USA
[e] Global Monitoring Division, Earth System Research Laboratory, NOAA, Boulder, CO, USA
[f] Space Vehicles Directorate, Air Force Research Laboratory, Hanscom Air Force Base, MA, USA
[g] NOAA National Climatic Data Center, Asheville, NC, USA
[h] Department of Geography, University of Wales Swansea, Swansea, UK

ARTICLE INFO

Article history:
Received 10 February 2009
Received in revised form 18 November 2009
Accepted 21 November 2009

Keywords:
MODIS
BRDF
Surface albedo
Validation
Spatial analysis
Remote sensing
SAFARI 2000 Project
EOS land validation core sites
NSA-Barrow
ARM-SGP Central Facility
MODTRAN

ABSTRACT

In this effort, the MODerate Resolution Imaging Spectroradiometer (MODIS) (Collection V005) Bidirectional Reflectance Distribution Function (BRDF)/Albedo algorithm is used to retrieve instantaneous surface albedo at a point in time and under specific atmospheric conditions. These retrievals are then used to study the role that the fraction of diffuse skylight plays under realistic scenarios of anisotropic diffuse illumination and multiple scattering between the surface and atmosphere. Simulations of the sky radiance using the MODTRAN®5.1 radiative transfer model were performed under different aerosol optical properties, illumination conditions, and surface characteristics to describe these effects on surface albedo retrievals from MODIS. This technique was examined using a validation scheme over four measurement sites with varied aerosol levels and landscapes, ranging from croplands to tundra ecosystems, and over extended time periods. Furthermore, a series of geostatistical analyses were performed to examine the types of spatial patterns observed at each measurement site. In particular, Enhanced Thematic Mapper Plus (ETM+) retrievals of surface albedo were acquired to analyze the change in variogram model parameters as a function of increased window-size. Results were then used to assess the degree to which a given point measurement is able to capture the intrinsic variability at the scale of MODIS observations. Assessments of MODIS instantaneous albedos that account for anisotropic multiple scattering, over snow-free and snow-covered lands and at all diurnal solar zenith angles, show a slight improvement over the albedo formulations that treat the downwelling diffuse radiation as isotropic. Comparisons with field measurements show biases improving by 0.004–0.013 absolute units (root-mean-squared error) or 0.1%–2.0% relative error.

Published by Elsevier Inc.

1. Introduction

Surface albedo describes the ratio of radiant energy scattered upward and away from the surface in all directions to the downwelling irradiance incident upon the surface. It is a key variable in regional and global radiation schemes, since it largely controls the amount of solar energy absorbed at the surface. Surface albedo is dependent on the Bidirectional Reflectance Distribution Function (BRDF), which describes the anisotropic reflectance of natural surfaces. Both surface albedo and the BRDF are determined by land surface structure, which influences the BRDF, for instance, by shadow casting, mutual view shadowing, and the spatial distribution of vegetation elements; and by surface optical characteristics, which determine the BRDF, for example, through vegetation–soil contrasts and the optical attributes of leaf scattering elements and the canopy reflectance. The spatial and temporal distribution of land surface properties, as seen in BRDF features, consequently reveal a variety of natural and human influences on the surface that are of interest to global change research (Lucht et al., 2000). As such, the accurate specification of satellite-derived albedos is important to earth system modeling efforts. Regional surface albedos with an absolute accuracy of 0.02–0.05 units (Henderson-Sellers & Wilson, 1983; Sellers et al., 1995) for snow-free and snow-covered land are required by climate, biogeochemical, hydrological, and weather forecast models at a diverse range of spatial (from 10s of meters to 5–30 km) and temporal (from daily to monthly) scales. Estimating albedos at intra-daily scales

* Corresponding author. Tel.: +1 301 614 5498; fax: +1 301 614 5269.
E-mail address: Miguel.O.Roman@nasa.gov (M.O. Román).

0034-4257/$ – see front matter. Published by Elsevier Inc.
doi:10.1016/j.rse.2009.11.014

also influences the accuracy of daily mean values of albedo. For instance a lack of consideration of the diurnal cycle of surface albedo yields an absolute error on the daily mean value of up to ±0.03 units, corresponding to 15% in relative terms (Grant et al., 2000). Similarly, Kimes et al. (1987) reported an 18% relative bias on the daily mean value of reflected solar irradiance.

Satellite remote sensing offers the only realistic means of monitoring surface albedo in a continental or global sense by providing spatially variable and temporally dynamic observations. With the launch of a number of polar orbiting sensors over the past decade, including MODIS, MISR, CERES, MERIS, and Parasol-POLDER, several global land surface albedo products are now being routinely produced. These datasets rely on multiple clear sky observations to characterize surface reflectance properties and must therefore contend with issues of cloud-clearing, snow detection, and aerosol correction as well as sensor-specific matters of view angle, spatial footprint, gridding, repeat cycles, and narrowband- to broadband conversion. These challenges have been successfully overcome in albedo-retrieving algorithms such as those of MODIS (Lucht et al., 2000; Schaaf et al., 2002, 2008; Wanner et al., 1997), MISR (Martonchik et al., 1998), and POLDER (Bacour & Breon, 2005; Buriez et al., 2007; Hautecoeur & Leroy, 1998; Maignan et al., 2004). Among these products, the MODIS V005 BRDF/albedo product provides intrinsic biophysical parameters of the surface, including surface reflectance anisotropy (BRDF model parameters), directional–hemispherical reflectance, and bihemispherical reflectance under isotropic illumination. These quantities are retrieved in seven narrow spectral bands between 0.4 and 2.4 μm as well as three broad bands encompassing the full solar range (0.3–5.0 μm) as well as the visible (0.3–0.7 μm) and shortwave infrared (0.7–5.0 μm) portions of that range.

To compare MODIS-derived surface albedo parameters with field-measured albedos, the MODIS intrinsic albedo quantities are normally combined as a simple weighted sum using the fractions of beam and diffuse illumination calculated for the observed optical depth and an appropriate atmospheric model using a Lambertian surface with a reflectance typical of the surface type (Lewis & Barnsley, 1994; Lucht et al., 2000). This formulation assumes that the directional distribution of sky radiance is unimportant since albedo involves an integration over illumination angles, and that albedo enhancement due to multiple interactions between the ground and atmosphere can be approximated within the definition of the diffuse proportion of illumination. This can lead to errors of a few percentages that have heretofore been ignored. Lewis and Barnsley (1994) noted that errors can increase under these assumptions at high solar zenith angles (SZA) and for atmospheres with high concentrations of aerosols. Pinty et al. (2005), have suggested that such errors can be as high as 10% (relative bias) under extremely turbid atmospheres and over strongly anisotropic surfaces. It is important to note that the MODIS V005 BRDF/albedo product is, nevertheless, a clear sky product. Thus, the algorithm was not designed to be specifically robust against conditions of increased haziness and at SZA>75°. Further, although there have been efforts to make sure that the underlying BRDF models operate well even at these higher zenith angles (Gao et al., 2001) and by other authors for the hotspot region (Maignan et al., 2004), the model parameters and hence the BRDF prediction relies on fitting to some limited set of satellite observations giving rise to uncertainty in the surface reflectance involved in any integral to albedo. Although earth system modelers have embraced the MODIS products and used them to refine their surface radiation parameterizations (Lawrence & Chase, 2007; Oleson et al., 2003; Wang et al., 2004; Zhou et al., 2003), they acknowledge that true land–atmosphere coupled albedos are also needed to gain a better understanding of the earth surface processes that they describe.

This paper addresses the specific role of anisotropic sky radiance and multiple scattering when using MODIS surface reflectance anisotropy products to reconstruct surface albedo at a point in time and under specific atmospheric conditions. A new method has been implemented to estimate instantaneous surface albedo, including the multiple scattering effects and the directional distribution of sky radiance. This method has been tested over a set of simulations using the MODTRAN®5.1 radiative transfer model (Berk et al., 2004). A number of test cases were also evaluated to determine robustness during periods of increased haziness. Results were then assessed against coincident field measurements over four field stations with landscapes ranging from croplands to tundra ecosystems and varied aerosol levels, to test the ability of the MODIS surface reflectance anisotropy data to capture the daily variability of surface albedo. Ground observations of surface albedo were obtained on an hourly basis during 3 to 5 year sampling periods using concurrent measurements of aerosol optical properties obtained by AErosol RObotic NETwork (AERONET) sunphotometers (Holben et al., 2001).

A spatial characterization of the MODIS V005 BRDF/albedo product was performed using 30 m Enhanced Thematic Mapper Plus (ETM+) albedo subsets as an intermediate between the satellite and point (tower) measurements. Although spatial scaling effects will always play a role in comparisons between coarse resolution satellite retrievals and fine resolution tower measurements, application of a geostatistical characterization of each site was also performed to indicate which measurement sites are most influenced by spatial scaling effects (in addition to any anisotropic effects). This approach improves the development and comparison of the proposed set of inversion techniques to estimate actual surface albedo from MODIS data.

2. Background

2.1. BRDF, albedo, and other definitions

The following is a summary of symbols and variables of interest related to BRDF and albedo, and remote sensing measurements. The definitions are linked to nomenclatures proposed by Nicodemus (1977) and reviewed in Liang (2004), Martonchik et al. (2000), and Schaepman-Strub et al. (2006):

Spectral and directional quantities:

$$\vartheta = \text{zenith angle} \tag{1}$$

$$\phi = \text{azimuth angle} \tag{2}$$

$$\Omega_s = \text{solar geometry} \tag{3}$$

$$\Omega_v = \text{viewing geometry} \tag{4}$$

$$\Omega_i = \text{incident geometry} \tag{5}$$

$$\lambda = \text{wavelength} \tag{6}$$

$$\Lambda = \text{waveband } \Lambda \text{ of width } \Delta\lambda \tag{7}$$

Atmospheric quantities:

$$L_\lambda\downarrow(\Omega_i) = \text{downwelling spectral radiance (at the ground) in direction } \Omega_i \tag{8}$$

$$L_{0\lambda}\downarrow(\Omega_i) = \text{downwelling spectral radiance at the bottom of the atmosphere over a totally absorbing lower boundary} \tag{9}$$

$$L_{0\lambda.Iso}\downarrow(\Omega_s) = L_{0\lambda}\downarrow(\Omega_i) \text{ under assumptions of isotropic diffuse illumination} \tag{10}$$

$$L_{0\lambda}(\Omega_i) = \text{downwelling diffusely – transmitted radiance at the bottom of the atmosphere for a totally absorbing lower boundary} \tag{11}$$

$\eta_\lambda\downarrow(\mu_s)$ = integral of $L_{0\lambda}(\Omega_i)$ over the sky illumination hemisphere (12)

$L_{sky\lambda}(\Omega_i)$ = downwelling sky radiance under Lambertian surface assumptions (13)

$E_{s\lambda}$ = exoatmospheric solar irradiance (14)

$\overline{\overline{\rho}}_\lambda$ = spherical albedo of the atmosphere for upward – travelling radiation (15)

$t_\lambda(-\mu_s)$ = downwelling direct transmittance of the atmosphere along the path from the Sun to the ground (16)

$T_\lambda(-\mu_s)$ = downwelling diffuse transmittance of the atmosphere along the path from the Sun to the ground (17)

$\gamma_\lambda(-\mu_s;\lambda,V)$ = total transmittance of the atmosphere along the path from the Sun to the ground (18)

D_λ = proportion of diffuse illumination (at the bottom of the atmosphere) (19)

$D_{0\lambda}$ = proportion of diffuse illumination for a totally absorbing lower boundary (20)

M_λ = degree of multiple scattering enhancement (21)

$N_{sky\lambda}(\Omega_i)$ = normalized sky radiance distribution under an absorbing lower boundary (22)

V = horizontal visibility (23)

$\beta_{Raleigh}$ = Raleigh scattering extinction coefficient at sea level (24)

τ = aerosol optical depth (AOD) at 550 nm (25)

Reflectance-based quantities:

R_λ = Lambertian surface reflectance (26)

$BRDF_\lambda$ = spectral bidirectional reflectance distribution function (BRDF) (27)

$R_\lambda(\Omega_v,\Omega_s)$ = spectral bidirectional reflectance factor (BRF) (28)

$f_{x,\Lambda}$ = RossThick – LiSparse Reciprocal (RTLSR) BRF kernel model parameter x (29)

$K_x(\Omega_v,\Omega_s)$ = RTLSR BRF model kernel x (30)

$\overline{K}_x(\Omega_v)$ = directional – hemispherical integral of $K_x(\Omega_v,\Omega_s)$ (31)

$\overline{\overline{K}}_x$ = bihemispherical integral of $K_x(\Omega_v,\Omega_s)$ (32)

$\overline{\overline{K'_{x\Lambda}}}$ = N_{sky}–weighted bihemispherical integral of $K_x(\Omega_v,\Omega_s)$

$\overline{\overline{K''_{x}}}_\Lambda(\Omega_s)$ = weighted sum of $\overline{K}_x(\Omega_v)$ and $\overline{\overline{K'_{x\Lambda}}}$ for a given atmospheric condition (33)

$\overline{\overline{K'''_{x}}}_\Lambda$ = the departure of $\overline{\overline{K'_{x\Lambda}}}$ with respect to $\overline{\overline{K}}_x$ (34)

Albedos:

$\overline{R}_\Lambda(\Omega_s)$ = directional – hemispherical integral of reflectance (black-sky albedo) (35)

$\overline{\overline{R}}_\Lambda$ = bihemispherical integral of reflectance (white-sky albedo) (36)

$\overline{\overline{R'}}_\Lambda$ = N_{sky}–weighted bihemispherical integral of reflectance (37)

$A_\Lambda(\vartheta_s)$ = surface albedo (full expression) (38)

$A_{\Lambda Iso}(\Omega_s)$ = surface albedo under assumptions of isotropic diffuse illumination (39)

2.2. Theoretical framework

The spectral Bidirectional Reflectance Distribution Function (BRDF) [sr^{-1}], an intrinsic property of a surface, describes the scattering of a parallel beam of incident light from one direction in the hemisphere into another direction in the hemisphere. It is defined as the ratio of the spectral radiance observed through an infinitesimally small solid angle cone, dL_λ [$W\,m^{-2}\,sr^{-1}\,\mu m^{-1}$], to the spectral irradiance illuminating that surface within an infinitesimal solid angle dE_λ [$W\,m^{-2}\,\mu m^{-1}$]:

$$BRDF_\lambda = \frac{dL_\lambda(\Omega_v,\Omega_s)}{dE_\lambda(\Omega_s)} \quad (40)$$

The spectral BRDF is a function of wavelength (λ) and the viewing and solar geometries (Ω_v, Ω_s), which are each defined by zenith and azimuthal angles (ϑ, ϕ). It is an intrinsic quantity that describes the directional way solar radiation reflects from the surface. It is more practical to consider the spectral Bidirectional Reflectance Factor (BRF) $R_\lambda(\Omega_v,\Omega_s)=\pi BRDF_\lambda$ (unitless), the ratio of the surface BRDF to that of a perfect Lambertian reflector with can be approximated by measurement over some (small) finite angle (with diffuse illumination and multiple interaction effects accounted for or assumed zero (Lyapustin & Privette, 1999)). We do not concern ourselves with the estimation of spectral BRF in this paper, but assume that this quantity can be approximated from some set of satellite, airborne, or ground-based measurements of spectral radiance or more usefully in the context of albedo estimation that such measurements have been used to parameterize a model of the BRF. Thus, the spectral BRF here is assumed an intrinsic surface property fully capable of describing the directional distribution of surface-leaving radiation as a function of wavelength.

The MODIS (Collection V005) BRDF/albedo product (Lucht et al., 2000; Schaaf et al., 2002, 2008) is derived from an algorithm that uses multi-date, atmospherically-corrected, samples of the spectral surface BRF of individual pixels over a 16 day period. In fact, these data are integrated over the MODIS wavebands and so no longer strictly spectral BRF but rather an approximation to this over the particular band set that we denote $R_\Lambda(\Omega_v,\Omega_s)$ over the waveband Λ though if the waveband is small, we can approximate this by $R_\lambda(\Omega_v,\Omega_s)$. We assume that all atmospheric influences have been removed from the BRF, making this an intrinsic surface property. The algorithm uses a reciprocal version of the semiempirical RossThick-LiSparse Reciprocal (RTLSR) kernel-driven BRF model (Lucht et al., 1999; Roujean et al., 1992; Wanner et al., 1995, 1997). This model is based on the theory that land surface reflectance can be decomposed into three major elements: (1) isotropic scattering, which is equal to the BRF for $\vartheta_v=\vartheta_s=0$; (2) volumetric scattering, so called for its development from scattering for a volumetric medium of oriented facets mimicking a leaf canopy (Ross, 1981); and (3) geometric-optical surface

scattering, which is derived for a sparse ensemble of surface objects casting shadows on a Lambertian background (Li & Strahler, 1992):

$$R_\Lambda(\Omega_v,\Omega_s) = f_{iso,\Lambda} + f_{vol,\Lambda}K_{vol}(\Omega_v,\Omega_s) + f_{geo,\Lambda}K_{geo}(\Omega_v,\Omega_s) \quad (41)$$

Here, K_{vol} is the coefficient for the RossThick volume scattering kernel; K_{geo} is the coefficient of the LiSparse Reciprocal geometric scattering kernel; and $f_{x,\Lambda}$ are the BRDF kernel model parameters x in waveband Λ with limits [Λ_{min}, Λ_{max}]. The MODIS V005 BRDF/albedo product attempts a full inversion retrieval of the parameters for the RTLSR BRDF model if sufficient high quality, cloud-free, and well distributed directional samples are acquired during a 16-day period. Otherwise, a magnitude inversion is performed when insufficient directional samples survive the screening process or if a robust full inversion retrieval cannot be made. In general it is always recommended that only high quality full inversion results be used, since they provide a higher quality of retrieved albedo than the magnitude inversion retrievals. However, Liu et al. (2009) recently found that the differences in quality, when combining both the full and magnitude methods retrievals, are often minor. The combination of MODIS Aqua and Terra sensor data has further increased the occurrence of high quality fully data-driven retrievals; thus reducing the product's reliance upon a priori determinations of the underlying surface anisotropy used by the backup algorithm (Salomon et al., 2006).

Surface albedo $A_\Lambda(\vartheta_s)$ is the ratio of upwelling to downwelling radiance integrated over an incident and surface-leaving upper hemisphere and the waveband:

$$A_\Lambda(\vartheta_s) = \frac{\frac{1}{\pi^2}\int_{\Lambda_{min}}^{\Lambda_{max}} d\lambda \int_0^{2\pi} d\phi_v \int_0^{2\pi} d\phi_i \int_0^1 d\mu_v \int_0^1 R_\lambda(\Omega_v,\Omega_i)L_\lambda\downarrow(\Omega_i)\mu_v\mu_i d\mu_i}{\frac{1}{\pi}\int_{\Lambda_{min}}^{\Lambda_{max}} d\lambda \int_0^{2\pi} d\phi_i \int_0^1 L_\lambda\downarrow(\Omega_i)\mu_i d\mu_i} \quad (42)$$

Here the integrations in the numerator are carried out over the waveband and all directions the surface scatters radiation into (the upper 'viewing' hemisphere, subscript v) and all directions the surface is illuminated from (the incident upper hemisphere, subscript i). For the denominator, the downwelling radiance is integrated over waveband and over all angles of the illuminating hemisphere (subscript i). Other terms in Eq. (42) are:

$$\mu_x = \cos(\vartheta_x) \quad (43)$$

$L_\lambda\downarrow(\Omega_i)$ [W m^{-2} sr^{-1} μm^{-1}] is the downwelling spectral radiance (at the ground) in direction Ω_i, due to direct and diffuse transmission of solar radiation through the atmosphere, enhanced by multiple interactions between the surface and atmosphere. Formulations for $L_\lambda\downarrow(\Omega_i)$ can be developed (e.g. Liang, 2004) by first considering $L_{0\lambda}\downarrow(\Omega_i)$ [W m^{-2} sr^{-1} μm^{-1}], the downwelling spectral radiance at the bottom of the atmosphere over a totally absorbing lower boundary:

$$L_{0\lambda}\downarrow(\Omega_i) = L_{0\lambda}(\Omega_i) + \frac{\mu_s E_{s\lambda} t_\lambda(-\mu_s)}{\pi} \quad (44)$$

where $L_{0\lambda}(\Omega_i)$ [W m^{-2} sr^{-1} μm^{-1}] is the downwelling diffusely-transmitted radiance at the bottom of the atmosphere in direction Ω_i for a totally absorbing lower boundary, $E_{s\lambda}$ [W m^{-2} μm^{-1}] is the exoatmospheric solar irradiance, $t_\lambda(-\mu_s)$ is the (downwelling) direct transmittance of the atmosphere along the path from the Sun to the ground, and μ_s is the cosine of the solar zenith angle. Note that the integral of $L_{0\lambda}(\Omega_i)$ over the sky illumination hemisphere $\eta_\lambda\downarrow(\mu_s)$ is:

$$\eta_\lambda\downarrow(\mu_s) = \frac{1}{\pi}\int_0^{2\pi} d\phi_v \int_0^1 L_{0\lambda}(\Omega_v)\mu_v d\mu_v = \frac{\mu_s E_{s\lambda} T_\lambda(-\mu_s)}{\pi} \quad (45)$$

where $T_\lambda(-\mu_s)$ is the downwelling diffuse transmittance of the atmosphere, so that for assumptions of isotropic diffuse illumination:

$$L_{0\lambda,Iso}\downarrow(\Omega_s) = \frac{\mu_s E_{s\lambda}\gamma_\lambda(-\mu_s)}{\pi} \quad (46)$$

where $\gamma_\lambda(-\mu_s;\lambda,V) = t_\lambda(-\mu_s) + T_\lambda(-\mu_s)$.

The illumination described in Eq. (44) is enhanced by multiple scattering between the surface and atmosphere:

$$L_\lambda\downarrow(\Omega_i) = L_{0\lambda}\downarrow(\Omega_i)\left(1 + \frac{\bar{R}_\lambda(\Omega_i)\bar{\bar{\rho}}_\lambda}{1-\bar{\bar{R}}_\lambda\bar{\bar{\rho}}_\lambda}\right) \quad (47)$$

where, $\bar{\bar{\rho}}_\lambda$ is the 'spherical albedo' (bihemispherical reflectance) of the atmosphere (for upward-travelling radiation), $\bar{R}_\lambda$ is the directional–hemispherical integral of reflectance and $\bar{\bar{R}}_\lambda$ is the bihemispherical integral of BRF.

Under Lambertian surface assumptions Eqs. (46) and (47) combine to give the downwelling sky radiance, $L_{sky\lambda}(\Omega_i)$, as stated by Liang (2004), after corrections replacing $\gamma(-\mu)$ by $\bar{\bar{\rho}}_\lambda$ in equation (2.116) of that text (Liang, 2009, pers. comm.):

$$L_{sky\lambda}(\Omega_i) = L_{0\lambda}(\Omega_i) + \left[\frac{R_\lambda\bar{\bar{\rho}}_\lambda}{1-R_\lambda\bar{\bar{\rho}}_\lambda}\right]\frac{\mu_s E_s\lambda}{\pi}\gamma_\lambda(-\mu_s) \quad (48)$$

where R_λ is the Lambertian surface reflectance. Note that Eqs. (47) and (48) assume the surface and atmosphere to be horizontally homogeneous.

We can define three key terms: (i) the proportion of diffuse illumination for a totally absorbing lower boundary $D_{0\lambda}$ (unitless):

$$D_{0\lambda} = \frac{T_\lambda(-\mu_s)}{t_\lambda(-\mu_s) + T_\lambda(-\mu_s)} \quad (49)$$

this being the same as the proportion of diffuse transmission; (ii) the degree of multiple scattering enhancement M (unitless):

$$M_\lambda = \frac{1}{1-\bar{\bar{R}}_\lambda\bar{\bar{\rho}}_\lambda} \quad (50)$$

and (iii) the normalized sky radiance distribution (under an absorbing lower boundary) N_{sky} (unitless):

$$N_{sky\lambda}(\Omega_i) = \frac{L_{0\lambda}(\Omega_i)}{\eta_\lambda\downarrow(\mu_s)}. \quad (51)$$

Note that the hemispherical integral of N_{sky} is unity. It follows from above that:

$$\frac{\pi L_\lambda\downarrow(\Omega_i)}{\mu_s E_{s\lambda}\gamma_\lambda(-\mu_s)} = [(1-D_{0\lambda}) + D_{0\lambda}N_{sky\lambda}(\Omega_i)][1 + \bar{R}_\lambda(\Omega_i)\bar{\bar{\rho}}_\lambda M_\lambda]. \quad (52)$$

If we assume all terms constant over some relatively narrow waveband of interest, the hemispherical integral of Eq. (52) (a scaled version of the denominator in Eq. (42)) then simplifies to:

$$\begin{aligned}\frac{\int_{\Lambda_{min}}^{\Lambda_{min}} d\lambda \int_0^{2\pi} d\phi_v \int_0^1 L_\lambda\downarrow(\Omega_v)\mu_v d\mu_v}{\mu_s E_{s\Lambda}\gamma_\Lambda(-\mu_s)} &= 1 + (1-D_{0\Lambda})M_\Lambda\bar{\bar{R}}_\Lambda\bar{\bar{\rho}}_\Lambda + D_{0\Lambda}M_\Lambda\bar{\bar{R}}'_\Lambda\bar{\bar{\rho}}_\Lambda \\ &= M_\Lambda(1 + D_{0\Lambda}\bar{\bar{\rho}}_\Lambda(\bar{\bar{R}}'_\Lambda - \bar{\bar{R}}_\Lambda)) \\ &\approx M_\Lambda.\end{aligned} \quad (53)$$

If we define $\bar{R}_\Lambda(\Omega_i)$ to be the directional–hemispherical integral of reflectance:

$$\bar{R}_\Lambda(\Omega_i) = \frac{1}{\pi}\int_0^{2\pi} d\phi_v \int_0^1 R_\Lambda(\Omega_v,\Omega_i)\mu_v d\mu_v \quad (54a)$$

then the bihemispherical integral of reflectance $\overline{\overline{R}}_\Lambda$ can be written:

$$\overline{\overline{R}}_\Lambda = \frac{1}{\pi}\int_0^{2\pi} d\phi_s \int_0^1 \overline{R}_\Lambda(\Omega_i)\mu_i d\mu_i \tag{54b}$$

and $\overline{\overline{R}}'_\Lambda$ is the N_{sky}-weighted bihemispherical integral of reflectance:

$$\overline{\overline{R}}'_\Lambda = \frac{1}{\pi}\int_0^{2\pi} d\phi_i \int_0^1 \overline{R}_\Lambda(\Omega_i)N_{sky\Lambda}(\Omega_i)\mu_i d\mu_i. \tag{54c}$$

The approximation given at the end of Eq. (53) relies on the difference of $\overline{\overline{R}}'_\Lambda - \overline{\overline{R}}_\Lambda$ being close to zero. Since these are both double integral terms and previous studies indicate that departures between single integrals of these functions are small up to around 70°, it is very likely that the difference between N_{sky}-weighted and unweighted double integrals over upper hemispheres will be very small.

Similar to the above analysis, the scaled numerator in Eq. (42) can be written:

$$\frac{\frac{1}{\pi}\int_{\Lambda_{min}}^{\Lambda_{max}} d\Lambda \int_0^{2\pi} d\phi_v \int_0^{2\pi} d\phi_i \int_0^1 d\mu_v \int_0^1 R_\lambda(\Omega_v,\Omega_i)L_{\lambda\downarrow}(\Omega_i)\mu_v\mu_i d\mu_i}{\mu_s E_{s\Lambda}\gamma_\Lambda(-\mu_s)} = [(1-D_{0\Lambda})\overline{R}_\Lambda(\Omega_s) + D_{0\Lambda}\overline{R}'_\Lambda]M_\Lambda. \tag{55}$$

From Eqs. (42), (53), and (55) we can define albedo:

$$A_\Lambda(\Omega_s) = \frac{[(1-D_{0\Lambda})\overline{R}_\Lambda(\Omega_s) + D_{0\Lambda}\overline{\overline{R}}'_\Lambda]}{1 + D_{0\Lambda}\,\overline{\rho}_\Lambda(\overline{\overline{R}}'_\Lambda - \overline{\overline{R}})} \tag{56a}$$

or, approximating $\overline{\overline{R}}'_\Lambda$ by $\overline{\overline{R}}$ as above:

$$A_\Lambda(\Omega_s) \approx [(1-D_{0\Lambda})\overline{R}_\Lambda(\Omega_s) + D_{0\Lambda}\overline{\overline{R}}'_\Lambda]. \tag{56b}$$

We see from this that albedo is a function of: (i) $D_{0\Lambda}$ the proportion of diffuse illumination (for an absorbing lower boundary); (ii) $\overline{R}_\Lambda(\Omega_s)$ the directional–hemispherical integral of reflectance (Eq. (54a) — the 'black-sky albedo'); (iii) $\overline{\overline{R}}'_\Lambda$ the bihemispherical integral of reflectance with a weighting of the normalized sky radiance (Eq. (54c)); and $\overline{\overline{R}}$ the bihemispherical integral of reflectance (Eq. (54b)), although only weakly a function of this latter term.

Eqs. (56a) and (56b) are rather interesting: although the multiple-scattered term is a potentially important component of the diffuse illumination, it has only minimal impact on the albedo if phrased like this. This is because the proportionate impact it has is the same for both the downwelling and upwelling radiation. Note that the proportion of diffuse illumination in these equations is that for illumination over a totally absorbing lower boundary. A *measured* value of this term (at the bottom of the atmosphere), D_Λ (unitless) will of course incorporate the multiple-scattered radiation and so will depart slightly from $D_{0\Lambda}$:

$$D_\Lambda(\Omega_s) = D_{0\Lambda}(1 - \overline{\overline{R}}_\Lambda\,\overline{\rho}_\Lambda) + \overline{R}_\Lambda(\Omega_s)\,\overline{\rho}_\Lambda. \tag{57}$$

To fully define albedo for the linear models of Eq. (41), we need to simply calculate the angular integrals (directional–hemispherical reflectance, bihemispherical reflectance and N_{sky}-weighted versions of this latter term). Because of the linear form of the BRF models these are just:

$$\begin{aligned}\overline{R}_\Lambda(\Omega_i) &= \frac{1}{\pi}\int_0^{2\pi} d\phi_v \int_0^1 R_\Lambda(\Omega_v,\Omega_i)\mu_v d\mu_v \\ &= f_{iso\Lambda} + f_{vol\Lambda}\overline{K}_{vol\Lambda}(\Omega_s) + f_{geo\Lambda}\overline{K}_{geo\Lambda}(\Omega_s)\end{aligned} \tag{58a}$$

$$\begin{aligned}\overline{\overline{R}}_\Lambda &= \frac{1}{\pi}\int_0^{2\pi} d\phi_i \int_0^1 \overline{R}_\Lambda(\Omega_i)\mu_i d\mu_i \\ &= f_{iso\Lambda} + f_{vol\Lambda}\overline{\overline{K}}_{vol\Lambda} + f_{geo\Lambda}\overline{\overline{K}}_{geo\Lambda}\end{aligned} \tag{58b}$$

$$\begin{aligned}\overline{\overline{R}}'_\Lambda &= \frac{1}{\pi}\int_0^{2\pi} d\phi_i \int_0^1 \overline{R}_\Lambda(\Omega_i)N_{sky\Lambda}(\Omega_i)\mu_i d\mu_i \\ &= f_{iso\Lambda} + f_{vol\Lambda}\overline{\overline{K}}'_{vol\Lambda} + f_{geo\Lambda}\overline{\overline{K}}'_{geo\Lambda}\end{aligned} \tag{58c}$$

where:

$$\overline{K}_x(\Omega_v) = \frac{1}{\pi}\int_0^{2\pi} d\phi_i \int_0^1 K_x(\Omega_v,\Omega_i)\mu_i d\mu_i \tag{59a}$$

$$\overline{\overline{K}}_x = \frac{1}{\pi}\int_0^{2\pi} d\phi_v \int_0^1 \overline{K}_x(\Omega_v)\mu_v d\mu_v \tag{59b}$$

$$\overline{\overline{K}}'_{x\Lambda} = \frac{1}{\pi}\int_0^{2\pi} d\phi_i \int_0^1 \overline{K}_x(\Omega_i)N_{sky\Lambda}(\Omega_i)\mu_i d\mu_i \tag{59c}$$

this latter term being the N_{sky}-weighted bihemispherical integral of the kernel x. Thus, from Eqs. (56a)–(56b) and (58a)–(58c):

$$A_\Lambda(\Omega_s) = \frac{[f_{iso\Lambda} + f_{vol\Lambda}\overline{\overline{K}}''_{vol\Lambda}(\Omega_s) + f_{geo\Lambda}\overline{\overline{K}}''_{geo\Lambda}(\Omega_s)]}{1 + D_{0\Lambda}\overline{\overline{\rho}}_\Lambda(f_{vol\Lambda}\overline{\overline{K}}'''_{vol\Lambda}(\Omega_s) + f_{geo\Lambda}\overline{\overline{K}}'''_{geo\Lambda}(\Omega_s))} \tag{60a}$$

$$A_\Lambda(\Omega_s) \approx f_{iso\Lambda} + f_{vol\Lambda}\overline{\overline{K}}''_{vol\Lambda}(\Omega_s) + f_{geo\Lambda}\overline{\overline{K}}''_{geo\Lambda}(\Omega_s) \tag{60b}$$

where:

$$\overline{\overline{K}}''_{x\Lambda}(\Omega_s) = (1-D_{0\Lambda})\overline{K}_x(\Omega_s) + D_{0\Lambda}\overline{\overline{K}}'_{x\Lambda} \tag{61a}$$

$$\overline{\overline{K}}'''_{x\Lambda} = \overline{\overline{K}}''_{x\Lambda} - \overline{\overline{K}}_x \tag{61b}$$

Eqs. (60a), (60b), (61a) and (61b) give us formulae for albedo that incorporate the directional influence of sky radiance and the multiple scattering effect between ground and atmosphere. Note that the denominator in Eq. (60a) is not a function of $f_{iso\Lambda}$ and that the impact of $f_{iso\Lambda}$ in the numerator is not conditioned by the proportion of diffuse radiation or the angular distribution of sky radiance. Albedo can be seen to be a function of (i) $D_{0\Lambda}$ the proportion of diffuse illumination (for an absorbing lower boundary); (ii) $\overline{K}_x(\Omega_s)$ the directional–hemispherical integral of kernel x (Eq. (59a) — cf. the 'black-sky albedo'); (iii) $\overline{\overline{K}}'_{x\Lambda}$ (Eq. (59c)) the bihemispherical integral of kernel x with a weighting of the normalized sky radiance; and $\overline{\overline{K}}_x$ the bihemispherical integral of kernel x (Eq. (59b)). The elegance of this is that these kernel integrals can be pre-computed for given assumptions regarding N_{sky} as a function of solar zenith angle and then albedo can be simply calculated for a given proportion of diffuse illumination from the BRF model parameters via Eqs. (60a) and (60b). Previously, these integrals had only been characterized for isotropic illumination conditions (i.e. $N_{sky}=1$) (e.g. Lucht et al., 2000). Under these conditions, $\overline{\overline{K}}_x = \overline{\overline{K}}'_{x\Lambda}$, so $\overline{\overline{K}}'''_{x\Lambda} = 0$ and:

$$\overline{\overline{K}}''_{x\Lambda Iso}(\Omega_s) = (1-D_{0\Lambda})\overline{K}_x(\Omega_s) + D_{0\Lambda}\overline{\overline{K}}_x \tag{62}$$

so albedo, $A_{\Lambda Iso}(\Omega_s)$, becomes:

$$\begin{aligned}A_{\Lambda Iso}(\Omega_s) = {} & f_{iso\Lambda} + (1-D_{0\Lambda})[f_{vol\Lambda}\overline{K}_{vol}(\Omega_s) + f_{geo\Lambda}\overline{K}_{geo}(\Omega_s)] \\ & + D_{0\Lambda}[f_{vol\Lambda}\overline{\overline{K}}_{vol}(\Omega_s) + f_{geo\Lambda}\overline{\overline{K}}_{geo}(\Omega_s)]\end{aligned} \tag{63}$$

i.e. a simple linear weighting between the 'black-sky albedo' (from the directional–hemispherical integrals of the kernels) and the 'white-sky albedo' (from the bihemispherical integral of the kernels). The difference between the isotropic statement (Eq. (63)) and the fuller expression (Eq. (60a)) is a function of: (i) the proportion of diffuse illumination (since if all illumination is direct there will be no impact from assumptions regarding the diffuse component); (ii) the RTLSR BRDF model parameters (since if the magnitude of the isotropic

parameter $f_{iso\Lambda}$ is much greater than the other parameters, the directional nature of the illumination will have limited impact as discussed above); and (iii) the terms $\overline{\overline{K}}'''_{x\Lambda} = \overline{\overline{K}}'_{x\Lambda} - \overline{\overline{K}}_x$ (since the closer this is to zero, the closer the albedo is to that under assumed isotropic diffuse illumination). This explains why earlier studies such as Lewis and Barnsley (1994) were able to show that assuming isotropic illumination for albedo (i.e. applying Eq. (63)) was robust other than for high solar zenith angles (where an increase in diffuse illumination is expected and also the directional nature of illumination may depart most strongly from the assumed isotropic form) and for rather turbid atmospheres (again, where the proportion of diffuse illumination will be greater). We might expect then the proportion of diffuse illumination to most strongly condition the departure of the fuller model of albedo from the isotropic illumination assumption. This will be a function of solar zenith angle and atmospheric optical thickness which we also describe in this paper (as primary input to MODTRAN®5.1) through V [km], the horizontal visibility:

$$V = \frac{\ln(50)}{\beta_{\text{Raleigh}} + \tau} \tag{64}$$

which is defined here as the distance over which the aerosol optical depth (AOD) at 550 nm, τ, is reduced to 2% using a Raleigh scattering extinction coefficient at sea level, $\beta_{\text{Raleigh}} \sim 0.01$.

In this section, we have developed three formulae for albedo (ignoring narrow-to-broadband issues throughout), namely Eqs. (60a), (60b) and (63). The first is a 'full' description of albedo incorporating the spectral and angular distribution of sky radiance as well as the impacts of multiple scattering between the ground and atmosphere. The second is an approximation to this that involves integrating the BRF kernels with a weighting for normalized sky radiance, and the third is based on the assumption that the sky radiance is isotropic. Whilst there might be some merit in exploring the second of these, we limit ourselves in this paper to comparing results between the 'full' expression (Eq. (60a)) and the 'isotropic' illumination expression (Eq. (63)).

Fig. 1 shows the diurnal variation of MODIS albedos (both intrinsic and instantaneous) as a function of SZA. MODIS black-sky albedos (Eq. (58a)) show a "U-shaped" trend that reach a minimum value around local solar noon time. Notice that the MODIS white-sky albedos remain constant while the N_{sky}-weighted expression varies throughout the day for different sky radiance distributions. Both the 'full' expression of actual albedo (Eq. (60a)) and the 'isotropic' illumination expression (Eq. (63)) are shown. Lucht et al. (2000) recognized that Eq. (63) makes a variety of simplifying assumptions about the nature of the diffuse radiation field, which should naturally respond to levels of increased haziness. Comparisons by Liu et al. (2009) between MODIS albedos and field measurements have also shown how this formulation produces a decreasing trend with underestimation as the SZA increases beyond 70°–75°. This trend is confirmed in Fig. 1, which shows how the isotropic expression consistently underestimates the tower data particularly during the early morning and late afternoon. Consequently, Eq. (63) has so far been recommended for SZA<70°. Since the MODIS black-sky albedo and white-sky albedo quantities represent the extreme cases under completely direct and completely diffuse illumination, the major challenge in deriving a more realistic estimate of actual albedo is to account for the angular dependencies and multiple-order scattering effects associated to the diffuse (sky) radiation field. Lyapustin and Privette (1999) introduced a method that essentially corrects for the diffuse component by coupling estimates of the sky radiance distribution with the modified function of the non-linear Rahman–Pinty–Verstraete BRDF model (MPRV) (Martonchik et al., 1998; Rahman et al., 1993). Their results confirm the importance in relating ground-measured reflectance to a 'true' bidirectional measurement to account for the anisotropic nature of the diffuse illumination. Accordingly, by characterizing the magnitude and angular distribution of the sky radiance, a new set of linear atmospheric kernel

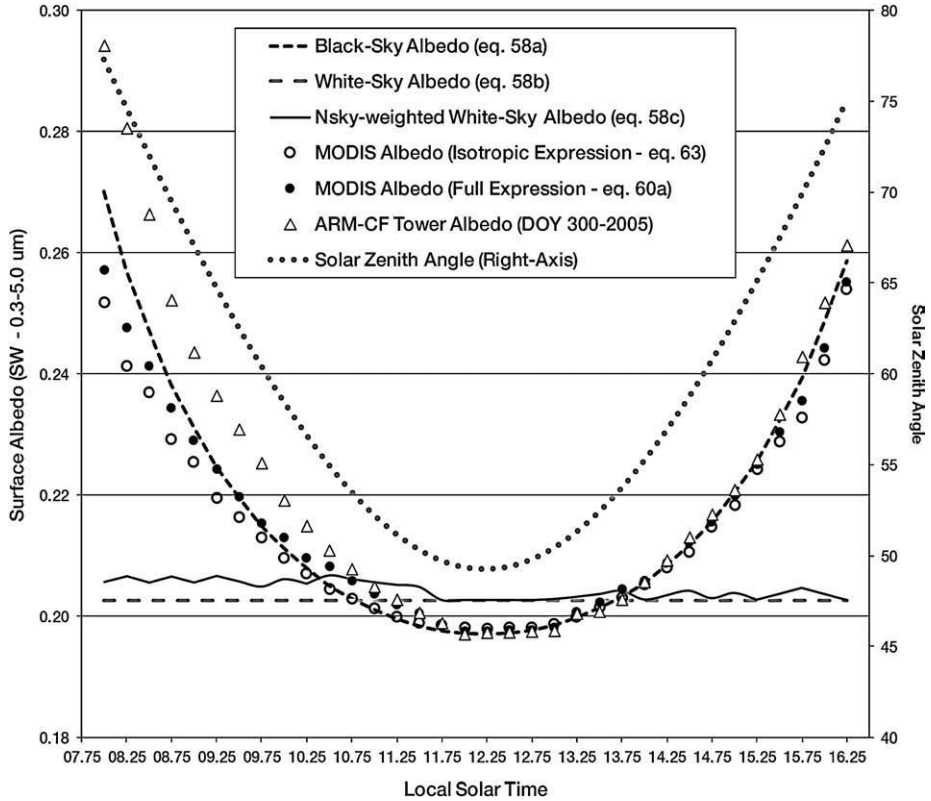

Fig. 1. MODIS intrinsic albedos (white-sky and black-sky) and actual albedos (isotropic and full expressions) shown as a function of solar geometry (solar time — SZA) compared against field measurements at the ARM-SGP Central Facility (ARM-CF) on 9/27/2005.

Table 1
Field measurements used from the Southern Africa Regional Science Initiative 2000 (SAFARI 2000) and the Atmospheric Radiation Measurements (ARM) Program.

Station name	Station ID	Latitude, longitude	Land-cover (Biome)	MODIS tile
SAFARI-Mongu	MON	15.438S, 23.253E	Shrubland/ woodland	H20V10
SAFARI-Skukuza	SKU	25.020S, 31.497E	Shrubland/ woodland	H11V04
ARM-NSA-Barrow	BAR	71.281N, 156.612W	Tundra	H12V01
ARM-SGP Central Facility	CF-01	36.605N, 97.488W	Grassland/ cereal crop	H10V05

integrals for the MODIS BRDF/albedo product are described above for any instantaneous surface–atmosphere scenario.

In this paper, the normalized sky radiance N_{sky} (Eq. (51)) is estimated under pristine conditions (i.e. no aerosols, $\tau=0$, or a horizontal visibility $V=391$ km), and, like L_{sky}, it is dependent on wavelength and solar geometry. The data used in the calculation of N_{sky} are generated by performing multiple MODTRAN®5.1 runs with differing view directions over the entire BRDF hemisphere (see Section 5). As with the original RTLSR kernel coefficients, these calculations can be pre-computed and stored in lookup tables encompassing numerous surface, illumination, and atmospheric scenarios. Results can then be combined with the existing set of linear equations to derive the 'full' description of albedo incorporating the spectral and angular distribution of sky radiance as well as the impacts of multiple scattering between the ground and atmosphere. The specific role of these factors in shaping the actual albedo (see Eqs. (60a), (60b), (61a) and (61b)) can be determined by computing $\overline{\overline{K}}'_{vol\Lambda}$ and $\overline{\overline{K}}'_{geo\Lambda}$. It is the departure of these two quantities (with respect to the original kernel bihemispherical integrals $\overline{\overline{K}}_{vol}$ and $\overline{\overline{K}}_{geo}$) that controls how well we can estimate the influence of the sky radiance on bidirectional reflectance and, consequently, obtain a more truly instantaneous albedo retrieval. Findings relating to these terms will be general in nature (for a given RTLSR kernel coefficient): the practical impact is thus a function of these and the particular RTLSR kernel parameters, $f_{x\Lambda}$, for a given canopy/surface scenario.

3. Field measurements

Data records from four study sites with available measurements of top-of-the-canopy broadband albedo, aerosol optical properties, and radiation fluxes were assembled for this study (Table 1). The goal was to measure the extent to which surface albedo values were being modulated, in part, by changes at the landscape level as well as by the presence of aerosols events. Since the model developed assumes the sky and ground reflectance to be horizontally homogeneous (in its treatment of the effects of multiple scattering) landscapes exhibiting extremely fragmented surfaces are likely to provide the greatest departure from this assumption and the poorest test of this component of albedo (as described here). The study sites were therefore selected based on their propensity to exhibit such spatial and temporal patterns at varying illumination conditions.

3.1. Southern Africa Regional Science Initiative 2000 (SAFARI, 2000)

Tower-based albedo measurements were collected over African savannas throughout the Southern Africa Regional Science Initiative 2000 (SAFARI, 2000; Swap et al., 2002). This international effort was established to explore, study, and address linkages between land–atmosphere processes and the relationship of biogenic, pyrogenic or anthropogenic emissions and the consequences of their deposition to the functioning of the biogeophysical and biogeochemical systems of Southern Africa. Data were collected by instrumentation deployed at the top of a 22 m tower at the Skukuza site in Kruger National Park, South Africa, and a 30 m tower in the Kataba Local Forest near Mongu, Zambia. Additional information about SAFARI 2000 can be found at (WWW1. SAFARI 2000 Project, 2000) (Privette et al., 2005). Surface BRDFs were also taken by the Cloud Absorption Radiometer (CAR) (King et al., 1986) over Mongu and Skukuza during SAFARI 2000 dry season campaign (Gatebe et al., 2003).

The Skukuza site (Fig. 2a) is located in the southern region of Kruger National Park in northeastern South Africa on a gently undulating landscape. The instrument tower was located between two distinct savanna types, a broad-leafed combretum savanna and a fine-leafed acacia savanna. Tree height was about 7–8 m on average. A dense grass layer covered the soil. The climate around Skukuza is semi-arid subtropical, with hot, rainy summers, warm dry winters, and an annual average rainfall of 550–650 mm. Temperature averages 26 °C in the dry season and 32 °C in the wet season. The natural disturbance regime of the site includes frequent fires (typically 3–8 yrs), as well as grazing and browsing by numerous species of wild ungulate.

The Mongu site (Fig. 2c) is located approximately 20 km south of Mongu in Western Province, Zambia. The Local Forest is a Zambezian woodland (miombo-like) on Kalahari Sands, about 11 m in height that undergoes subsistence harvesting. Mongu is situated at an elevation of 1187 m near the Zambezi River with a seasonality defined by wet and dry cycles. The rainy season extends from about November to April; and the dry season from about May to October. Temperature averages 30 °C in the dry season and 26 °C in the wet season. Annual rainfall averages 949 mm, occurring primarily in the wet season.

Both Mongu and Skukuza field stations contained Kipp and Zonen albedometers housing upward- and downward-looking pyranometers. These instruments were outfitted with clear and red domes to collect broadband albedo and radiation fluxes in the shortwave (SW) (0.3–2.8 μm) and near-infrared (NIR) (0.7–2.8 μm) wavebands, respectively. The data stored are mean values provided at 15-minute intervals from March 2, 2000 to December 31, 2002 for Mongu, and at 30-minute intervals from April 9, 2000 to December 31, 2002 for Skukuza. Photosynthetically active radiation (PAR) (0.3–0.7 μm) was calculated from measurements at both sites.

3.2. Atmospheric Radiation Measurement Program

Expanding observations networks to obtain the most useful climate data was a strong motivation of the Atmospheric Radiation Measurement Program (ARM) (Ackerman & Stokes, 2003; Zhanqing et al., 2003). With this goal in mind, an extensive field program was initiated in 1989 to obtain the necessary climate quality measurements, with a primary emphasis on the Southern Great Plains (SGP) region and a secondary emphasis in the Northern Slope of Alaska (NSA). Two ARM sites were chosen for this study: (1) the Central Facility (CF-01) in the Southern Great Plains (SGP) and (2) the NSA-Barrow facility. Data were collected by instrumentation deployed at the top of a 60 m tower at the Central Facility and atop a 20 m tower at the Barrow Facility.

The heavily instrumented Central Facility is located at the heart of the SGP on 160 ac of cattle pasture and wheat fields southeast of Lamont, Oklahoma (Fig. 2b). This station is situated at an elevation of 1014 m with temperatures averaging 34.7 °C in the summer and −5.0 °C in the winter seasons. The climate is classified as sub-humid with an average annual rainfall of 750 mm. The harvest of winter wheat is particularly interesting in the SGP region, as during this period, most of the land is converted from waist-high winter wheat to bare soil in a matter of hours. The timing of this harvest occurs in early June and depends, among several factors, on seasonal climate trends, recent precipitation, and the availability of migrating harvesting equipment. Drastic changes in surface albedo associated with these impulse-like surface perturbations have important implications for the structure and occurrence of cumulus convection; which tend to trigger other feedback

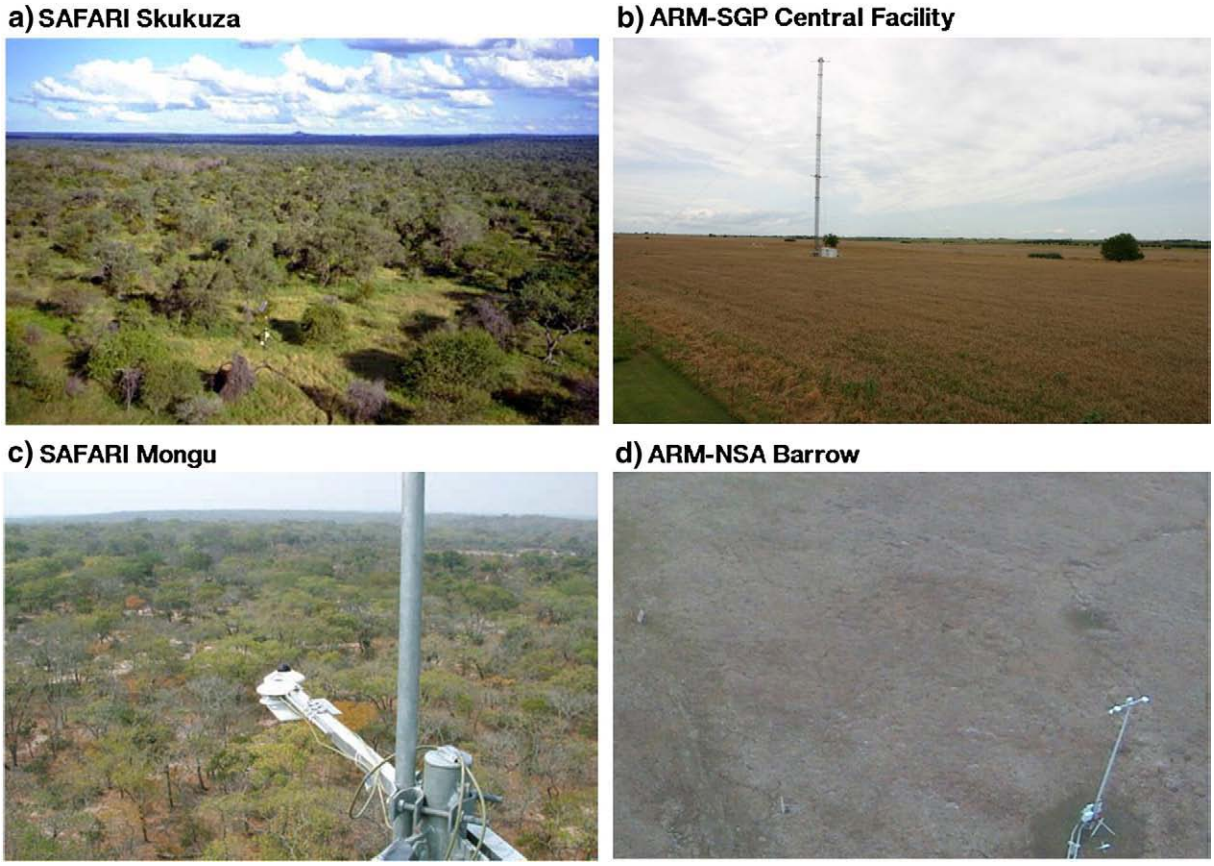

Fig. 2. Field stations at (a) Skukuza, South Africa taken from a 22 m tower, 24 March 2000, (b) the ARM-Central Facility (Lamont, Oklahoma) taken at the base of the 60 m tower, 20 June 2007, (c) Mongu, Zambia taken from a 33 m tower, 2 September 2000, and (d) Barrow, Alaska taken from a 40 m tower, 27 August 2008. Images (a–b) courtesy of Jeff Privette (NOAA). Image (d) courtesy of DOE-ARM.

effects (e.g. increases in evapotranspiration and stomatal resistance) on these intensive agricultural landscapes (Cosh, 2007).

The NSA-Barrow site (Fig. 2d) is located over arctic tussock tundra, wet sedge, and wet/moist meadows about 8 km northeast of the village of Barrow, Alaska. An arctic climate is present in Barrow with an average annual precipitation of 127 mm, including snowfall of approximately 508 mm. Temperatures range from −45.5 °C to 27 °C throughout the year. Barrow also experiences 24 h of day light, or an average SZA of 60° for approximately 3 months during the summer. Conversely, 3 months of darkness occurs during the winter months. Although measurements at this station are made over open tundra, the Arctic Ocean is about 3 km northwest of the site. Because of its proximity to the ocean and prevailing east–northeast winds off the Beaufort Sea, this site is perhaps best characterized as having an Arctic maritime climate affected by variations of weather and sea ice conditions in the Central Arctic. During the summer of 2004, forest fires destroyed vast areas of boreal forest in Alaska and western Canada, releasing smoke into the atmosphere. Smoke aerosol passing over the NSA-Barrow station was monitored by sunphotometers to determine its physical and optical properties and its impact on the surface radiation budget. Radiative forcing at the top-of-the-atmosphere (TOA) throughout this event was especially sensitive to small changes in surface albedo. Results in Stone et al. (2005, 2008) show how periods of increased haziness can reduce the net shortwave flux at TOA by about 30 W m^{-2} over the ocean while at the same time increasing it by 20 W m^{-2} over an adjacent area of melting sea ice, all in the vicinity of the Barrow site.

Both the ARM-CF-01 and NSA-Barrow stations have Kipp and Zonen tower albedometers. These instruments are outfitted with clear domes to collect broadband albedo and radiation fluxes in the shortwave (SW) (0.3–2.8 μm) waveband. Two additional instruments, a normal incidence pyrheliometer mounted on an automatic sun tracker and a shaded pyranometer riding on top of the sun tracker, measure direct and diffuse solar radiation incident upon the field stations. Estimates of cloud fraction as viewed from skyward-looking pyranometers were also used. The data stored are mean values provided at 30-minute intervals from January 1, 2003 to December 31, 2005 for the Central Facility and for January 1, 2002 to December 31, 2007 for the Barrow site. Data from these two stations is available at the Clouds and the Earth's Radiant Energy System (CERES) ARM Validation Experiment (CAVE) archive (WWW2. CAVE HOME PAGE, 2009) (Rutan et al., 2001).

3.3. AErosol RObotic NETwork (AERONET)

The AERONET (AErosol RObotic NETwork) program is a federation of field-based remote sensing aerosol networks that standardizes instruments, calibration, and data processing (Holben et al., 2001). AERONET sun photometers measure the intensity of sunlight arriving directly from the sun and sky at preprogrammed (~hourly) intervals for the retrieval of AOD at 550 nm and water vapor amounts, particle size distribution, aerosol scattering, phase function, and single scattering albedo. Level 2 AOD data available from AERONET sunphotometers were collocated at each of the measurement sites (Fig. 3). These measurements have undergone pre- and post-field calibration and have been automatically cloud cleared and manually inspected.

4. Spatial characterization

In order to understand the effects of scale on the accuracy of surface albedo retrievals from MODIS, high-resolution ETM+ scenes

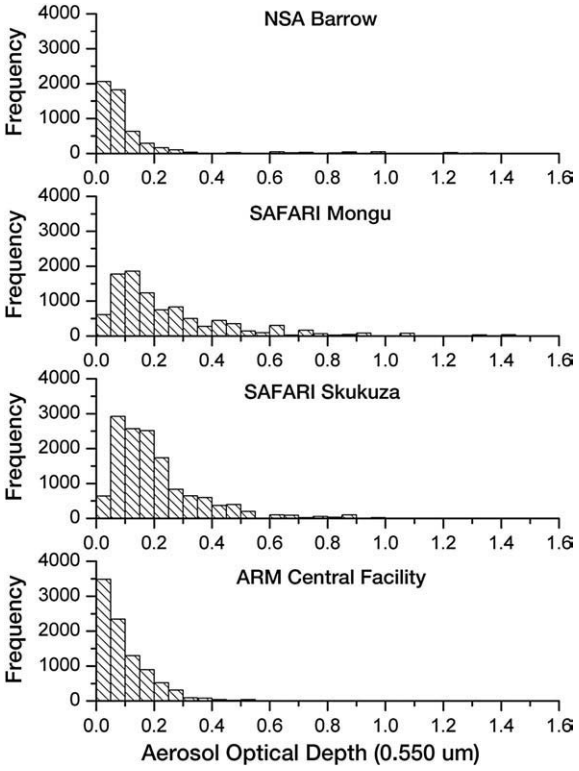

Fig. 3. Histograms displaying the frequency distribution of 550 nm aerosol optical depths (AOD) estimated from AERONET sun photometers at preprogrammed ~hourly intervals over NSA-Barrow (2002–2007), SAFARI-Mongu (2000–2002), SAFARI-Skukuza (2000–2002), and the ARM-SGP Central Facility (2003–2005).

were used to assess the degree of spatial representativeness between a given point (tower) measurement and the surrounding landscape extending to a MODIS spatial grid (Román et al., 2009). The methodology for estimating broadband albedos based on empirical relations between surface total shortwave albedo measurements and ETM+ observations is discussed in further detail in Liang (2001). Table 2 compares field measurements against MODIS and 30 m Enhanced Thematic Mapper Plus (ETM+) albedo subsets over all study sites, using 253 m, 278 m, 417 m, and 758 m circular footprints for ARM-NSA-Barrow, SAFARI-Skukuza, SAFARI-Mongu, and the ARM-SGP Central Facility, respectively. Direct comparisons between ground observations and MODIS retrievals returned slightly lower RMSEs than their ETM+ counterparts. Hence, the surrounding region extending to the MODIS spatial grid, particularly over ARM-Central Facility and NSA-Barrow, slightly differs to the landscape elements that are within the ground-measured albedometer field of view (FOV). Although most of the RMSE scores were well within the appropriate range of quality assurance (i.e. all RMSE values were < (0.02–0.05) units of albedo), this spatial heterogeneity may at times lead to higher absolute RMSE values, particularly when changes in the surrounding landscape are more pronounced.

Table 2
Comparisons between field-measured albedos, MODIS V005 500 m blue-sky albedos, and ETM+ albedo subsets with matching footprints over each field station (i.e. 226 m, 249 m, 374 m, and 680 m circular footprints for ARM-NSA-Barrow, SAFARI-Skukuza, SAFARI-Mongu, and the ARM-SGP Central Facility, respectively).

Station name	Ground albedo	MODIS 500 m/(RMSE)	ETM+/(RMSE)
SAFARI-Mongu	0.1335	0.1425/(0.0090)	0.1537/(0.0202)
SAFARI-Skukuza	0.1580	0.1610/(0.0030)	0.1314/(0.0266)
ARM-NSA-Barrow	0.1251	0.1088/(0.0163)	0.0982/(0.0269)
ARM-SGP Central Facility	0.1753	0.1810/(0.0057)	0.1517/(0.0236)

One of the most efficiently used geostatistical tools for describing the spatial variability of primary biophysical properties is the semivariogram (Carroll & Cressie, 1996; Davis, 1986; Isaaks & Srivastava, 1989). Using high spatial resolution datasets enables efficient monitoring of the properties of semivariograms and can further reveal interesting spatial patterns of the landscape. The methodology for deriving semivariogram functions to analyze surface albedos using ETM+ subsets as intermediates between the ground-based and MODIS footprints was recently introduced by Susaki et al. (2007). In this work, the variogram estimator in Eq. (65) is used to obtain half the average-squared-difference between albedo values that are within certain distance classes or bins defined by multiples of 30 m (i.e. the nominal spatial resolution of an ETM+ pixel).

$$\gamma_E(h) = 0.5 \cdot \frac{\sum_{i=1}^{N(h)} (z_{xi} - z_{xi+h})^2}{N(h)} \tag{65}$$

where: z_x is the surface albedo at pixel location x; and z_{x+h} is the surface albedo at another pixel within a lag distance h. The spatial attributes a (range), c (sill), and c_0 (nugget effect) on can then be modified to fit an isotropic spherical variogram model (Materon, 1963) to the variogram estimator:

$$\gamma_{sph}(h) = \begin{cases} c_0 + c \cdot \left[1.5 \cdot \frac{h}{a} - 0.5 \frac{h^3}{a}\right] & \text{for } 0 \le h \le a \\ c_0 + c & \text{for } h > a \end{cases}. \tag{66}$$

Of particular interest is the range of the spherical variogram, a, which defines the distance from a point beyond which there is no further correlation of a given measurement associated with that point. Following the analysis by Susaki et al. (2007), the application of spherical variogram models using ETM+ data has been extended by analyzing the variogram model parameters as a function of increased window-size. This provides a means to account for all the possible surface covers that may contribute to the directional signatures acquired by the MODIS instrument throughout a 16-day period. By examining the range of the spherical variogram at different spatial resolutions, the ground-based footprints at each of the study sites can be compared against the larger landscapes extending to a satellite pixel; thus allowing us to examine the suitability of a measurement site for use in direct validation of actual albedo retrievals from MODIS.

Results of the semivariogram functions, and the relevant spatial attributes (range, sill, and nugget-effects), using ETM+ subsets over the measurement sites are shown in Figs. 4 and 5. Results show that the surface conditions inside the footprints of the ARM-Central Facility and NSA-Barrow measurement sites are significantly different from the surrounding regions extending to the MODIS 500 m footprint. Looking at the semivariogram functions, only the variogram range (a) (under 1.5 km) was <500 m over SAFARI-Skukuza, but >500 m at the ARM-Central Facility, SAFARI-Mongu, and NSA-Barrow field stations. Both the ground instruments over SAFARI-Skukuza and the ARM-Central Facility were overlooking a large circular footprint (i.e. ~278 m for SAFARI-Skukuza and a ~758 m at the ARM-Central Facility); but only over Skukuza, the footprint was larger in size than the obtained range values using the 1.5 km ETM+ subsets (i.e. ~274 m for Skukuza and ~818 m for ARM-Central Facility). The range of the semivariogram was also larger than the tower-measured footprints by ~219 m over SAFARI-Mongu, and by ~699 m over NSA-Barrow. The fact that the semivariance increased as a function of the spatial footprint, at the ARM-Central Facility and ARM-NSA-Barrow sites, further confirms the presence of an underlying trend; thus suggesting that a direct comparison between the tower-based estimates of surface albedo and the MODIS retrievals may introduce spatial scaling errors.

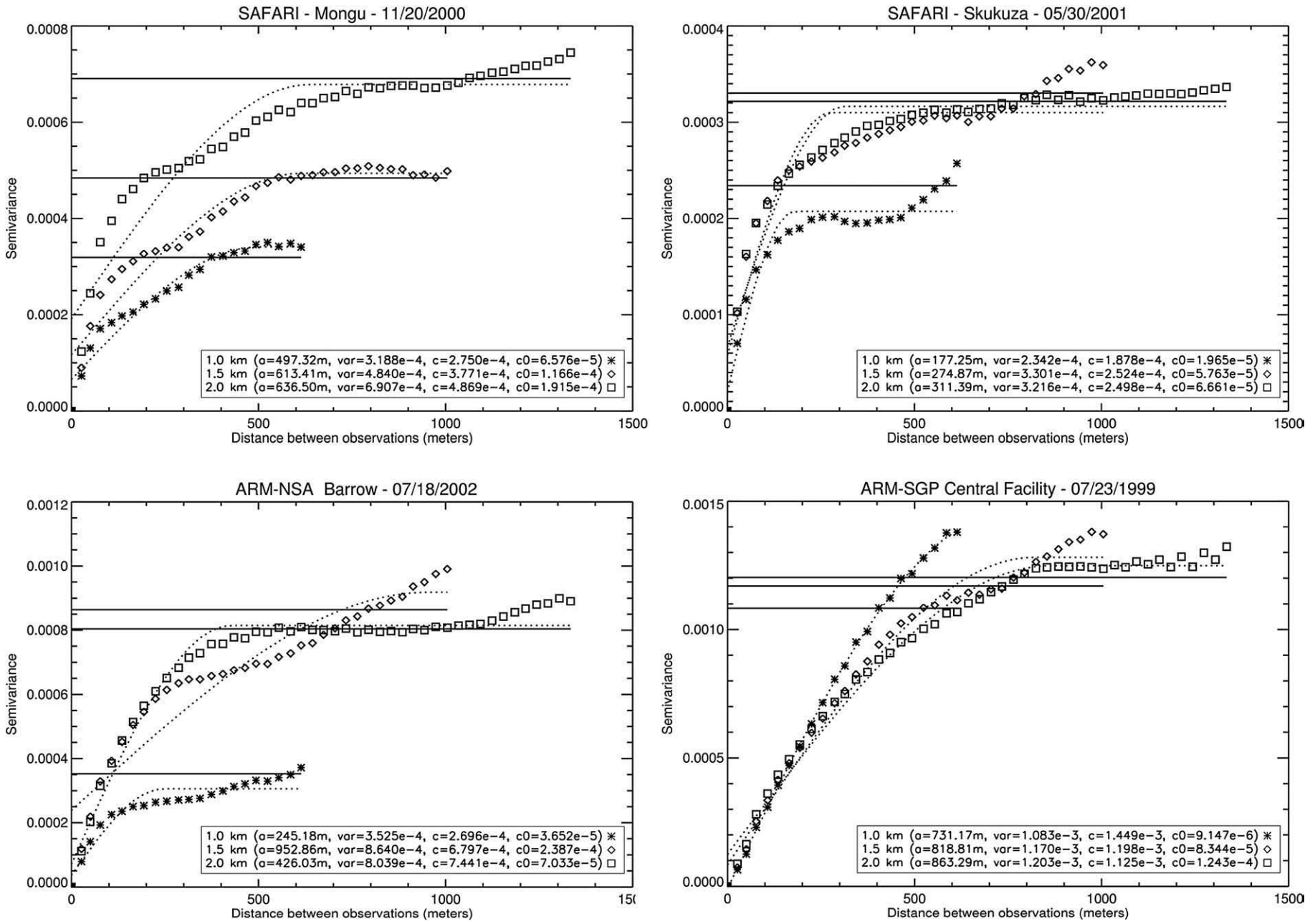

Fig. 4. Variogram estimator (points), isotropic spherical variogram model (dotted curves), and sample variance (solid straight lines) obtained over SAFARI-Mongu (top-left), SAFARI-Skukuza (top-right), ARM-NSA-Barrow (bottom-left), and ARM-SGP Central Facility (bottom-right) using surface albedos derived from ETM+ scenes (using 1.0 km, 1.5 km and 2.0 km subsets) collected on 20 November 2000, 30 May 2001, 18 July 2002, and 23 July 1999, respectively.

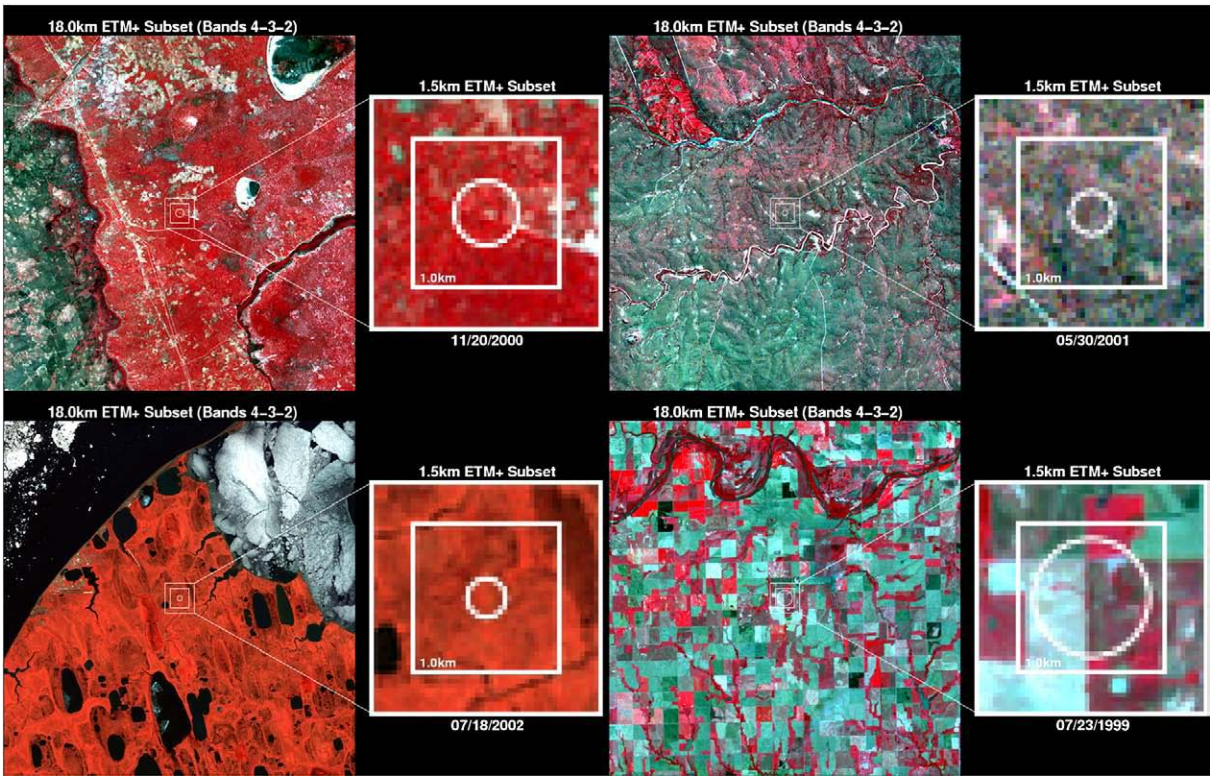

Fig. 5. Top-of-atmosphere reflectance (ETM+ Bands 4,3,2) subsets using 18.0 km, 1.5 km, and 1.0 km boundaries; all centered on the tower (circular) footprints at the SAFARI-Mongu (top-left), SAFARI-Skukuza (top-right), ARM-NSA-Barrow (bottom-left), and ARM-SGP Central Facility (bottom-right). At the Skukuza site, the lighter stretch inside the subset is a dirt road crossing Kruger National park. At the Central Facility, the region shows a cluster of agricultural fields ranging from winter wheat (including stubble) and pasture. At the Mongu site, the lighter colors are kalahari sands from abandoned agricultural sites along the northeastern edge of the Kataba Forest. The other larger patches of tan, cyan, and off-white are also sandy areas with more active cropping. In the larger (18 km × 18 km) subset near the village of Mongu (to the northwest), the off-white areas are roads and small buildings. The large lakes are dambos, which are shallow, seasonally flooded areas. At the Barrow site, the darker spots within and surrounding the 1.5 km boundaries are small swaps and bogs that are part of a larger network of tundra ponds and puddles that cover the southwestern edge of the study area. In the larger subset, the village of Barrow is seen about 3 km west of the field station and a cluster of ice-sheets floating over Elson Lagoon just east of the field station.

5. MODTRAN®5.1 simulations

The Moderate Resolution Transmittance radiative transfer model, MODTRAN®5.1 (Berk et al., 2004), provides the accuracy required for modeling and processing spectral measurements of distinct surface properties under any given atmospheric scenario. This version includes many new capabilities introduced specifically to enhance and facilitate atmospheric compensation due to anisotropic diffuse illumination and multiple scattering between the surface and atmosphere (Berk & Anderson, 2008). In particular, a new MODTRAN®5.1 atmospheric correction data output file includes a number of radiative transfer quantities required to calculate the sky radiance distribution. These include the downwelling diffusely-transmitted radiance at the bottom of the atmosphere (Eq. (11)), the spherical albedo of the atmosphere (Eq. (15)), as well as the downwelling direct and downwelling diffuse transmittance of the atmosphere along the path from the Sun to the ground (Eqs. (17) and (18), respectively). These data are computed by the DISORT multiple scattering algorithm (Stamnes et al., 1988, 2000) within MODTRAN®5.1. Here, diffuse transmittance is defined as the fraction of collimated radiation that passes through a medium after being scattered at least once (Chandrasekhar, 1960; Stamnes, 1982).

MODTRAN®5.1 characterizes the angular distribution of the diffuse component provided an aerosol model, absorbing gas concentration, horizontal visibility, and the view and solar geometries (Ω_v, Ω_s) are specified. With knowledge of these parameters, both the exoatmospheric solar irradiance (Eq. (14)) and the additional radiance due to Rayleigh scattering, aerosol attenuation, ozone and water vapor absorption can be calculated. Once the spectral range (of solar and sky radiation), illumination, and atmospheric conditions have been identified, their corresponding parameters can be used to compute and store the new set of linear atmospheric kernel integrals, $\overline{\overline{K}}'_{vol\Lambda}$ and $\overline{\overline{K}}'_{geo_\Lambda}$ (functions of solar zenith angle, since the sky radiance distribution changes with this), along with the unweighted integrals $\overline{K}_{vol}(\Omega_s)$, $\overline{K}_{geo}(\Omega_s)$, $\overline{\overline{K}}_{vol}$ and $\overline{\overline{K}}_{geo}$. Accordingly, a new set of 7 lookup tables were created (one for each of the MODIS visible and shortwave infrared wavebands) using 21 atmospheric visibility values for different aerosol loadings (ranging from 2.0 to 391 km), and 2 atmospheric profiles (i.e. Mid-Latitude Summer/Winter) that represent different water vapor and other gaseous amounts and profiles. A large range of viewing and illumination conditions were simulated, including SZAs ranging from 0°–80° with the increment of 1°, and a range of 9 view-zenith (from 0°–80°) and 37 relative azimuth angles (from −180°–180°). In total, 7,930,062 cases were simulated in MODTRAN®5.1 using an increasing wavelength increment from 0.0025 μm at the shortest wavelength end to 0.025 μm at the longest wavelength end.

Fig. 6 shows the MODIS Nadir BRDF-Adjusted Reflectance (NBAR) spectra for the most common seasonal surface conditions observed at each of the study sites. These spectral signatures were used to evaluate the ability of the new set of lookup tables to characterize the departure between the isotropic and full expressions of: (1) the bihemispherical integrals of reflectance (i.e. white-sky albedo); (2) the new set of linear atmospheric kernel integrals; and (3) the isotropic statement (Eq. (63)) and full expression of MODIS actual albedo (Eq. (60a)).

Fig. 7 illustrates the relative bias between the unweighted and N_{sky}-weighted versions of white-sky albedo (i.e. $\%Diff = (\overline{\overline{R}}'_\Lambda - \overline{\overline{R}}_\Lambda) \div \overline{\overline{R}}'_\Lambda$) for the surface conditions presented in Fig. 6. It is

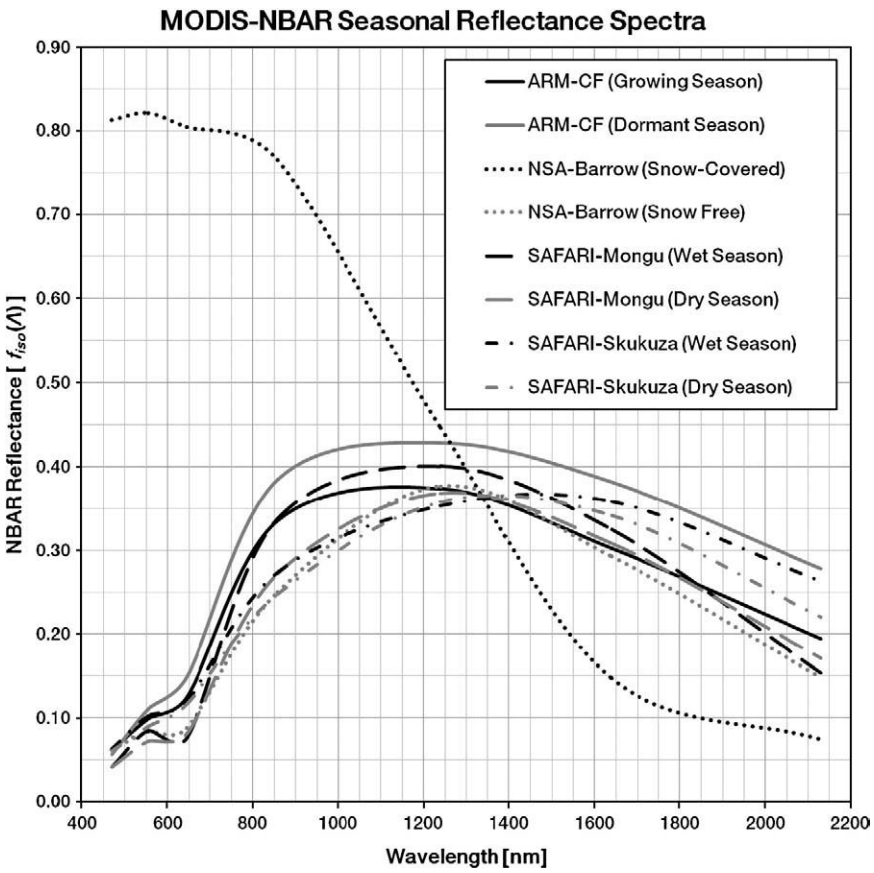

Fig. 6. MODIS Nadir BRDF-Adjusted Reflectance (NBAR) spectra, including the visible and shortwave infrared bands (Bands 1–7), for the most common seasonal surface conditions observed at each of the study sites.

the difference between Eqs. (59b) and (59c) that conditions the departure of MODIS white-sky albedo from isotropic diffuse illumination assumptions. Each of the seven MODIS 'land' bands (channels 1–7) are shown as a function of AOD. Results show the relative biases generally increasing as a function of AOD and decreasing as a function of wavelength. Most wavebands followed a linearly increasing trend corresponding to conditions of increasing haziness. In particular, the visible bands reached maxima ($\%Diff_{max}$) of 12%, 13%, and 18% in the Blue (Band #3), Green (Band #4), and Red (Band #1) bands, respectively. The NIR region showed a maximum of 7% and 11%, for Bands #2 and #5 (respectively), during the growing season at the ARM-Central Facility (Fig. 7a). The effects of anisotropic diffuse illumination were often minor across all sites for AODs<0.5 ($\%Diff_{max}$<6%), over snow-covered lands ($\%Diff_{max}$<4%) (see Fig. 7c), and in the 1628–2155 nm shortwave domain (i.e. Bands #6 and #7) ($\%Diff_{max}$<3%).

Fig. 8 illustrates Eq. (61a) (right plots) and Eq. (62) (left plots), for the MODIS red and NIR wavebands, over a range of AODs and solar zenith angles. Since Eq. (62) is mostly described by the original kernel integrals, $\overline{K}_x(\Omega_v)$ and $\overline{\overline{K}}_x$, this expression exhibits minimal spectral dependence. Conversely, Eq. (61a) is influenced by the spectral and angular distribution of the sky radiance. In particular, the red band experienced a notable increase in the magnitudes of $\overline{\overline{K}}''_{vol}$ and $\overline{\overline{K}}''_{geo}$ across all SZAs. The response was similar in the NIR band, albeit with a narrower increase in magnitude as a function of AOD. A key finding of this exercise is that explicit characterization of the influence of anisotropic diffuse illumination removes the biases between kernel integrals in the 55–60° SZA range. This range is shown to be insensitive to changes in AOD under conditions of isotropic illumination; which results in intrinsic albedo quantities (i.e. black-sky and white-sky) with equal magnitudes (see Fig. 5 in Lucht et al., 2000).

Figs. 9 and 10 illustrate the relative bias between the isotropic statement (Eq. (63)) and full expression of MODIS actual albedo (Eq. (60a)) under the most common seasonal surface conditions observed at the ARM-Central Facility and NSA-Barrow (Fig. 9); and over SAFARI-Mongu and SAFARI-Skukuza (Fig. 10). Each plot illustrates the change in broadband albedo at different aerosol optical depths. Since changing atmospheric conditions strongly influence the partitioning of direct and diffuse solar irradiance, the simulated change in actual albedo is well recognized. Over snow-covered lands, however, the effects on the relative bias followed a constant SZA trend and varied only as a function of AOD. While there is a marked response across the VIS and NIR broadbands, it is only when integrating over the full solar range that both the effects of anisotropic diffuse illumination and multiple scattering can be resolved as a function of changing surface conditions. These trends are demonstrated in Fig. 10, where the SW broadband experienced relative biases with bounds in upwards of 10.0–11.5%. These biases generally agree with the model-based albedo reconstructions in Pinty et al. (2005). It is important to emphasize that these findings only apply to retrieval scenarios under very turbid atmospheres and strongly anisotropic surfaces; and do not reflect the true (daily and seasonal) variability of MODIS albedo retrievals as a whole. As documented in Fig. 3, only a small fraction of the multi-year measurement periods (~1.75% for AODs>0.75 and 0.50% for AODs>1.0) fell under such extreme conditions. More realistically, our simulations and validation results (see Section 6) confirm that the assumption of isotropic diffuse illumination, as compared to actual albedos that closely represent instantaneous surface conditions, will instead lead to relative biases with bounds ranging from a minimum of 0.65% in the NIR (for SZA<50° and AODs<0.5) to a maximum of 5.69% in the SW domain (for SZA>70° and AODs>0.5).

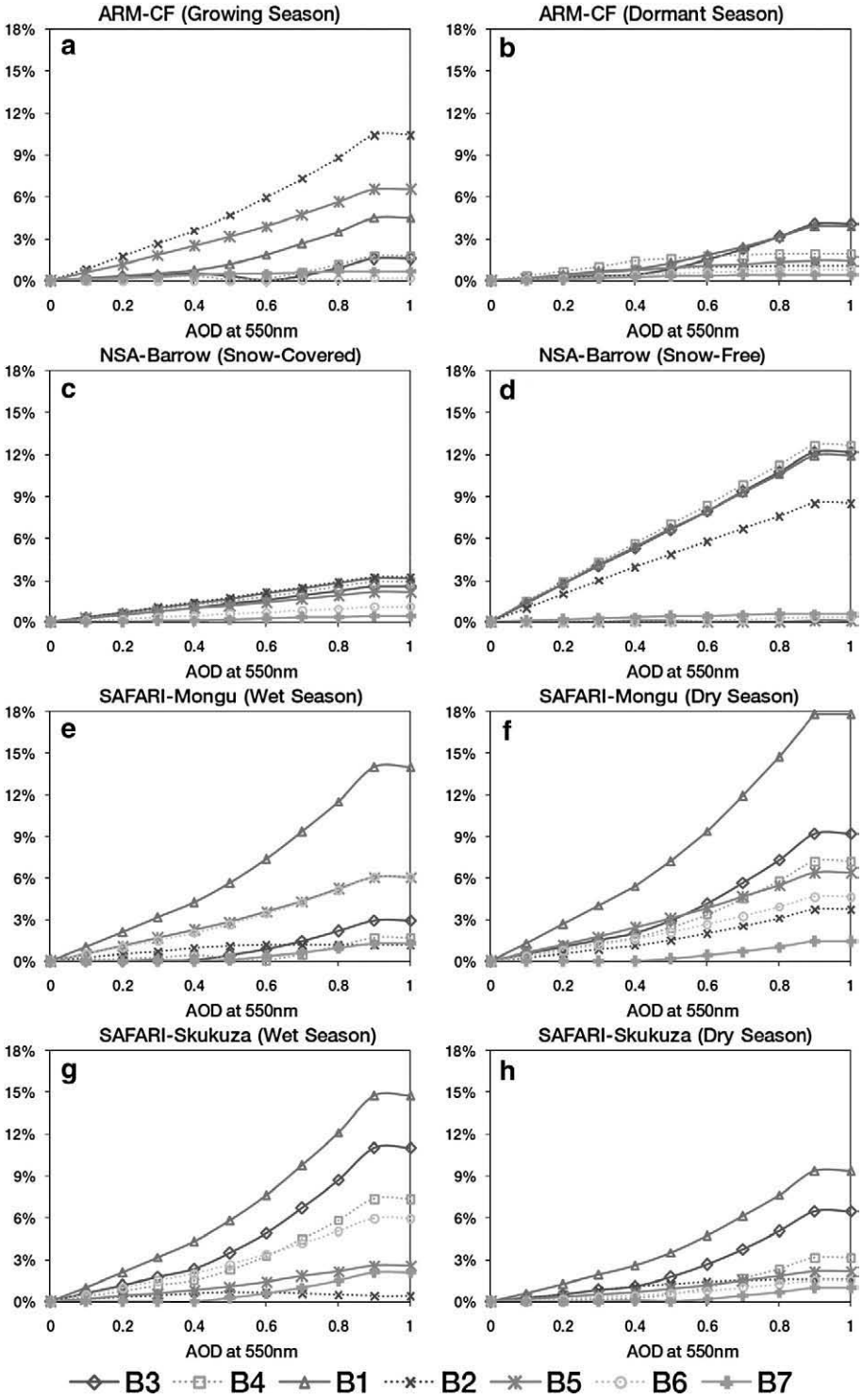

Fig. 7. Relative difference between the bihemispherical integrals of reflectance (Eqs. (59b) and (59c)), shown as a function of wavelength (for MODIS Bands 1–7) and aerosol optical depth (AOD) for the height of the growing and dormant seasons at the ARM-Central Facility (a–b); during snow-free and snow-covered periods at the NSA-Barrow measurement site; (c–d); and throughout the height of the dry and wet seasons at the SAFARI-Mongu (e–f) and SAFARI-Skukuza (g–h) measurement sites.

6. Validation results and discussion

Fig. 11 shows a 16-day period in 2005 at the ARM-Central Facility of cloud-free field measurements of surface albedo compared against MODIS retrievals using both the isotropic statement (Eq. (63)) and the full expression of actual albedo (Eq. (60a)). The ground retrievals of aerosol optical depth (AOD) at 550 nm are also plotted (right-axis). Because the atmospheric conditions remained constant throughout this period (with AOD values <0.2) both formulations responded the same throughout the day, with the full expression oftentimes obtaining improved estimates at the highest SZAs.

Fig. 12 shows a 21-day period in 2002 at the SAFARI-Skukuza measurement site. Both the isotropic and full expression of MODIS actual albedo systematically underestimated the ground albedos, particularly throughout the early mornings. This effect might have been caused by a non-leveled albedometer setup. It was very

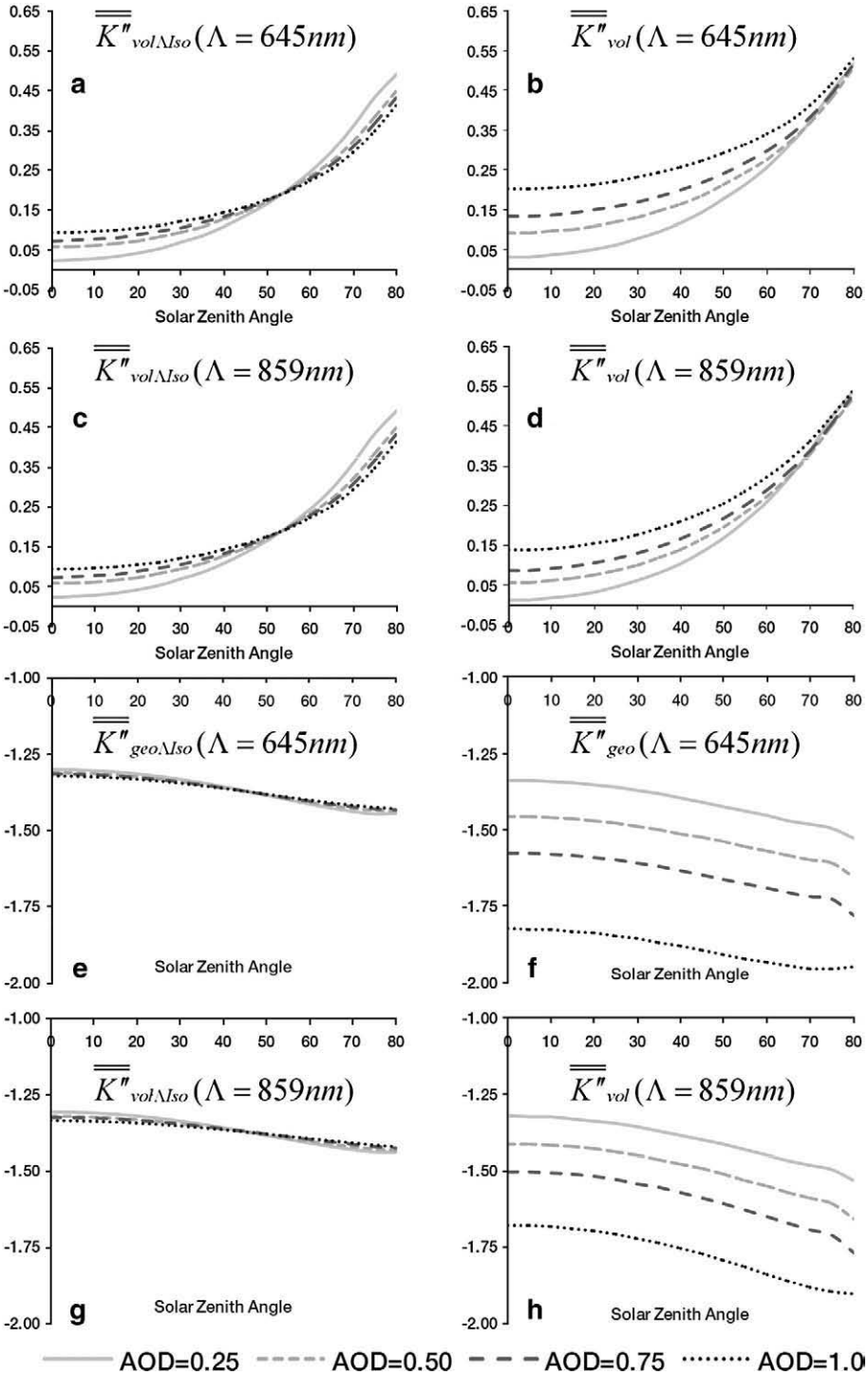

Fig. 8. Comparisons between Eq. (61a) (right plots) and Eq. (62) (left plots) for the MODIS red (645 nm) and the near-infrared (859 nm) wavebands over a range of AODs and solar zenith angles.

challenging to level the instrument, particularly as the Skukuza tower seemed to lean outwards. Thus, this problem may have overestimated the tower albedo by overexposing the upward-looking portion to the direct-beam as the solar disk approached the eastern horizon. Both formulations, however, improved over periods approaching local solar noon; with slightly better estimates for the full expression over periods of increased AOD and higher SZAs.

Fig. 13 shows a 25-day period in 2002 of cloud-free measurements of surface albedo at the NSA-Barrow measurement site compared against MODIS retrievals that were reconstructed for the same time period. Fig. 14 shows a 38-day retrieval period, also over Barrow, in 2004. Both figures illustrate different surface conditions (i.e. a period of snow-cover on Fig. 13 and snow-free conditions on Fig. 14), and include aerosol coupling events in which the AOD increased significantly by 1.0–2.5. These events resulted from the advection of Asian dust in 2002 (Stone et al., 2005) (Fig. 13) and smoke from boreal fires in 2004 (Stone et al., 2008) (Fig. 14). Throughout the measurement period in 2002, the NSA-Barrow measurement site also experienced an average SZA = 69°. The diurnal trend of surface albedo consequently deviated from the usual "U-shaped" trend that

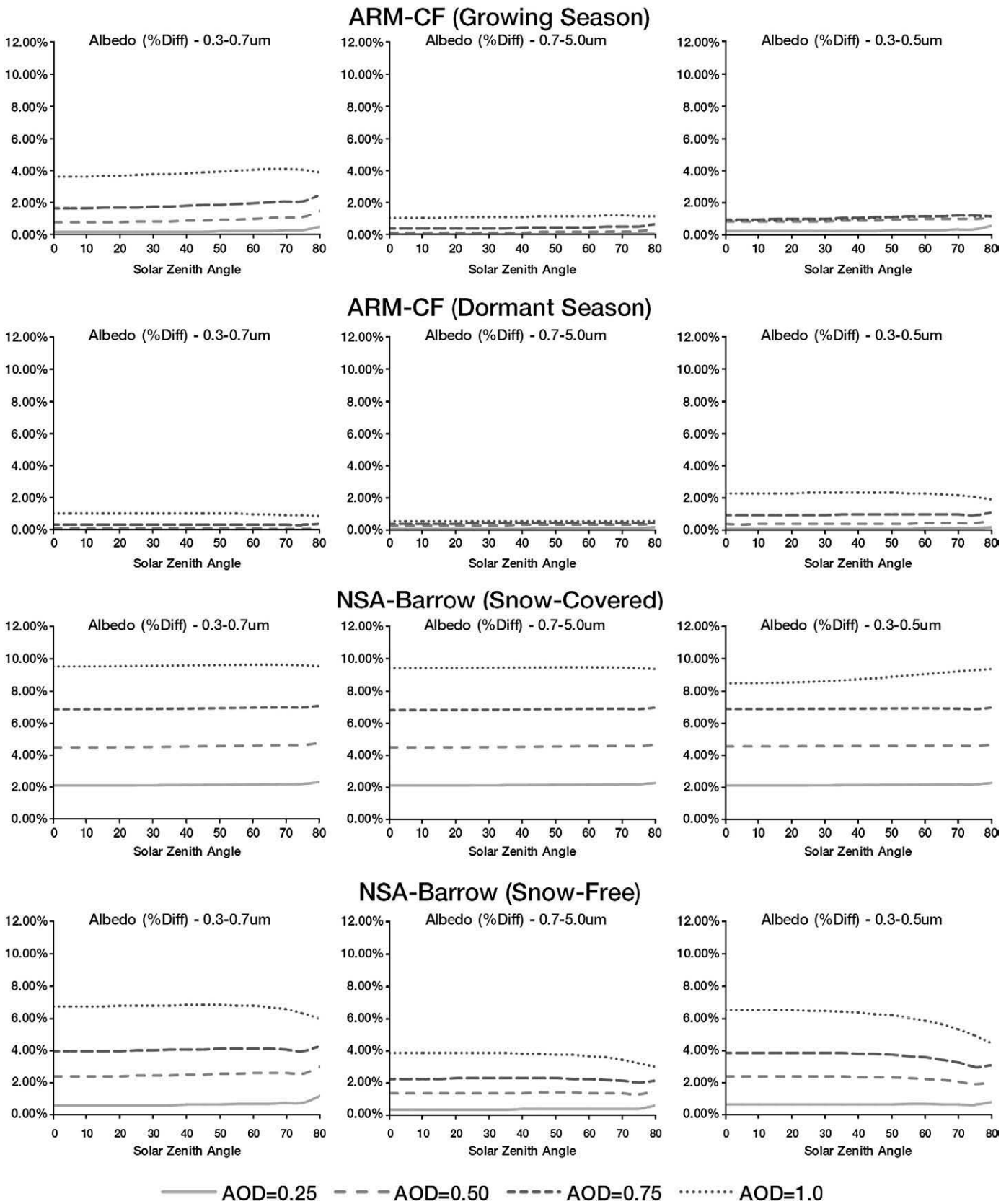

Fig. 9. Percent difference between the isotropic statement (Eq. (63)) and full expression of MODIS actual albedo (Eq. (60a)). The plots are shown as a function of solar zenith angle, using broadband albedo values in the visible (0.3–0.7 μm), shortwave infrared (0.7–5.0 μm), and full solar range (0.3–5.0 μm) (left, center, and right plots, respectively). Each curve illustrates the change in broadband albedo at different aerosol optical depths. The representative BRDFs are based on different seasonal conditions observed at the ARM-Central Facility and the NSA-Barrow measurement site.

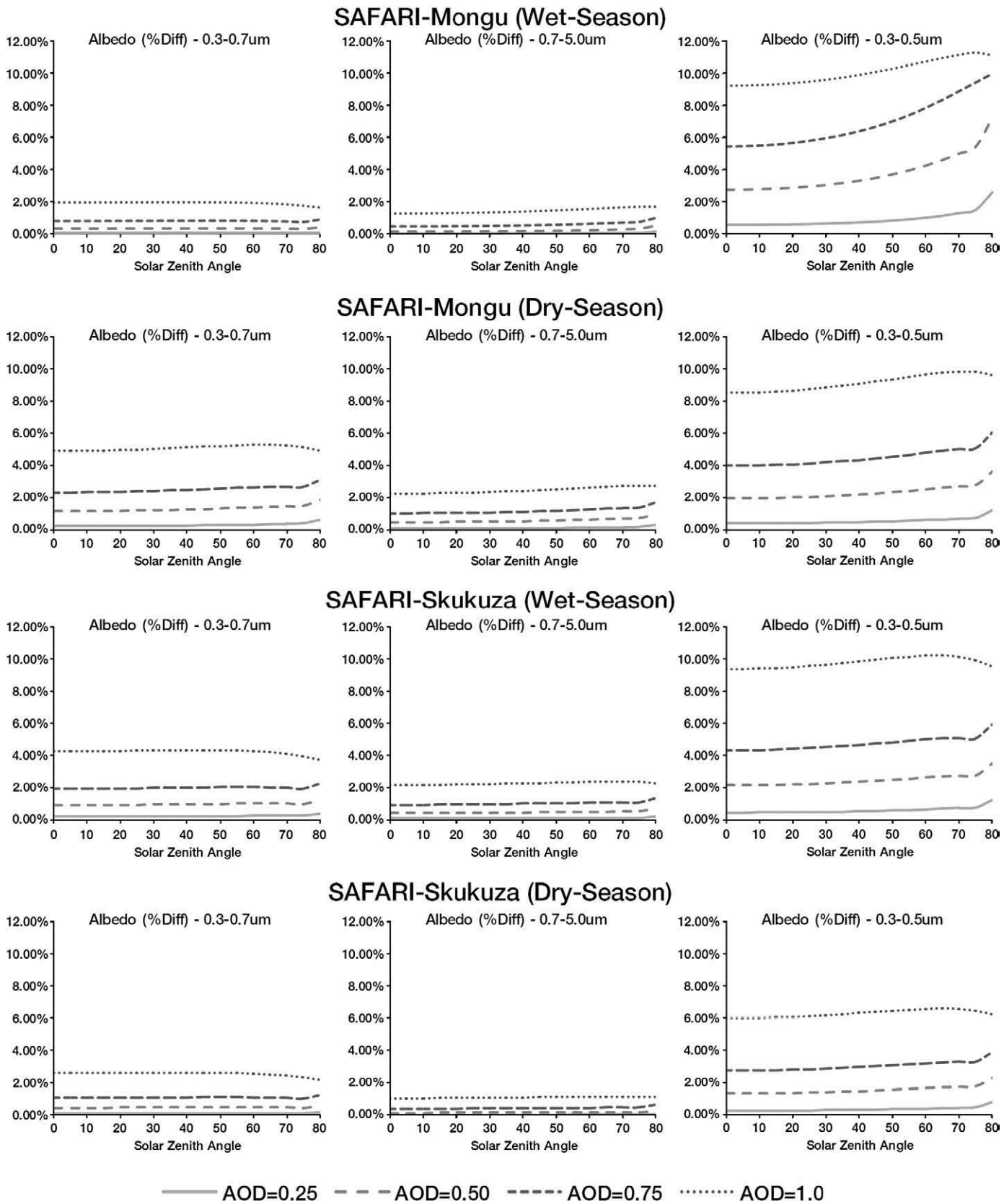

Fig. 10. Simulated change between (Eq. (63)) and (Eq. (60a)). The representative BRDFs are based on different seasonal conditions observed at the SAFARI-Mongu and SAFARI-Skukuza measurement sites. Setup is the same as Fig. 9.

reaches a minimum value around local solar noon time. The full expression of MODIS actual albedo performed very well, particularly over the 2 mentioned periods of increased haziness. However, the new formulation overestimated the tower measurements on various instances. Since the full expression of actual albedo attempts to correct for the effects of surface/atmosphere multiple scattering, there

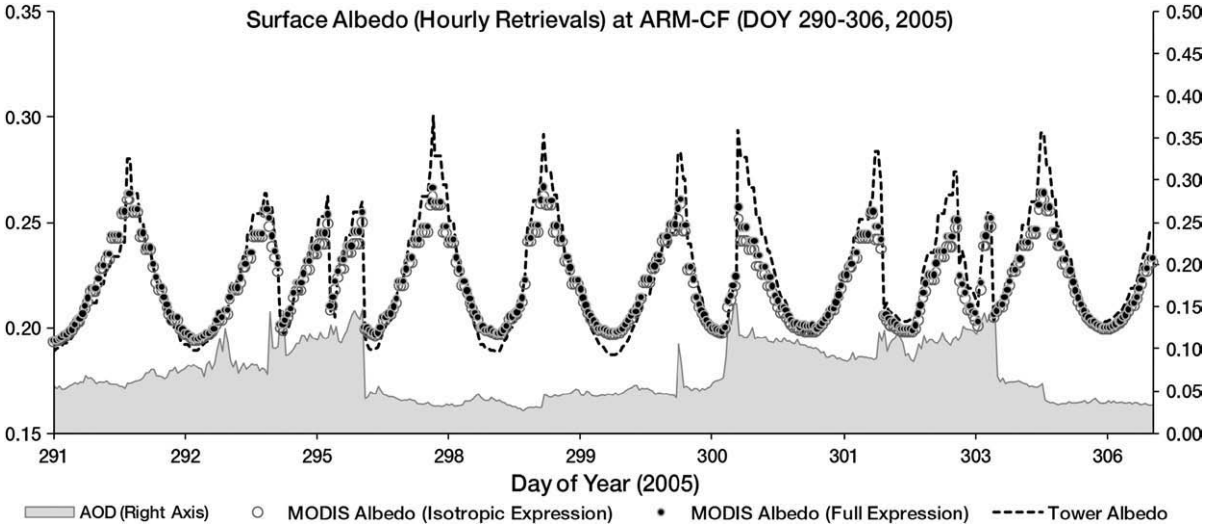

Fig. 11. (Left-axis) Diurnal change in surface albedo (SW — 0.3–5.0 μm) from tower measurements and MODIS retrievals (using both isotropic and full expressions) during DOY 290–306, 2005 at the ARM-Central Facility. (Right-axis) Coincident retrievals of aerosol optical depth at 550 nm from the local AERONET sunphotometer.

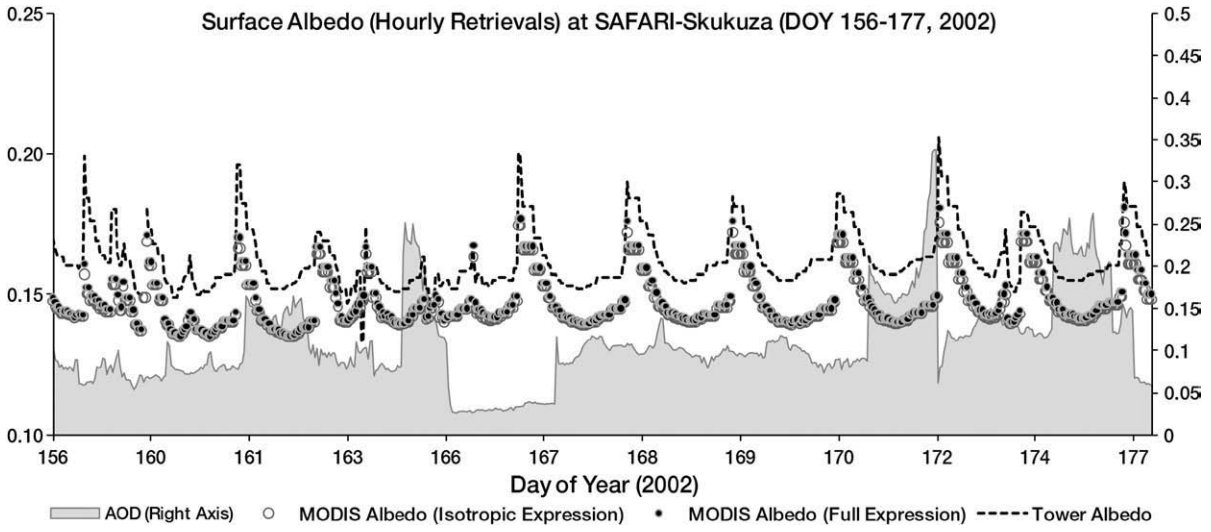

Fig. 12. Diurnal change in surface albedo during DOY 156–177, 2002 at the SAFARI-Skukuza measurement site. Setup is the same as Fig. 11.

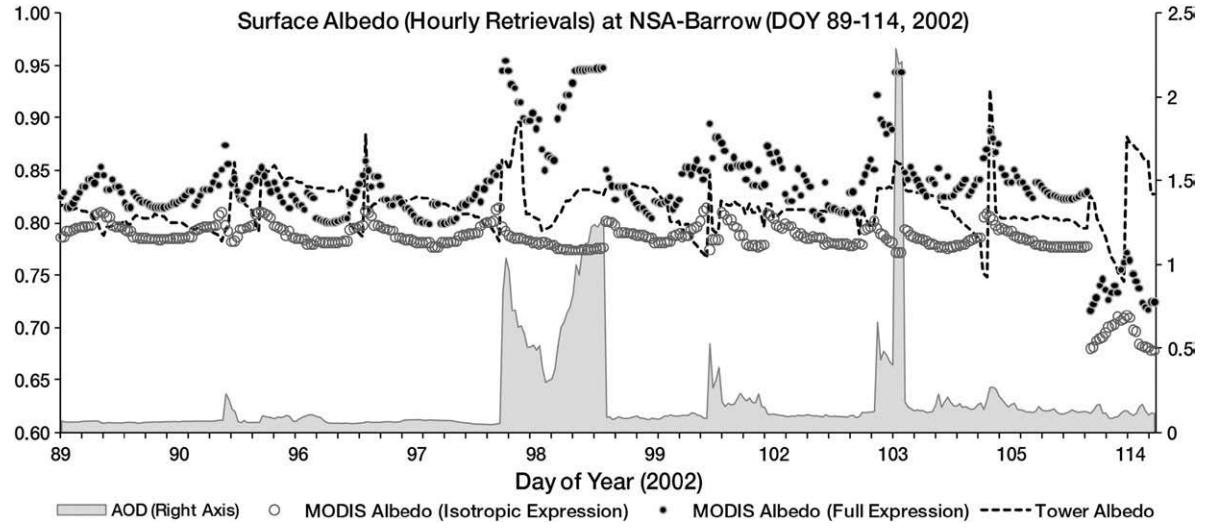

Fig. 13. Diurnal change in surface albedo during DOY 89–114, 2002 at the NSA-Barrow measurement site. Setup is the same as Fig. 11.

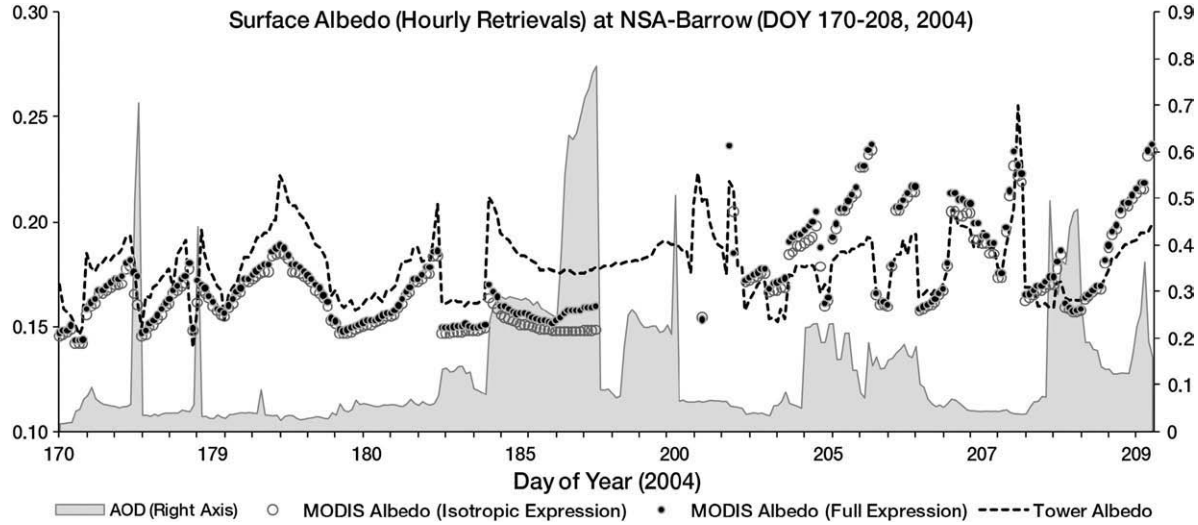

Fig. 14. Diurnal change in actual albedo during DOY 170–208, 2004 at the NSA-Barrow measurement site. Setup is the same as Fig. 11.

will be occasions whereby a sudden change in the underlying BRDF may occur in concurrence with high levels of AOD; thus, producing a slight overestimation in the actual albedo retrievals from MODIS. The surface reflectance anisotropy and albedo for a given MODIS pixel are thus governed by the predominant conditions during a multi-date period (in this case 16 days). Any rapidly changing surface conditions that may dramatically lower the albedo (e.g. snow-melt periods over NSA-Barrow) will thus affect the overall quality of the full expression of actual albedo until the MODIS algorithm reacts to such changes and applies a new BRDF retrieval on subsequent periods. More frequent retrievals with preferential weighting of the most recent observation will somewhat mitigate this lag but archive constraints have thus far limited this retrieval strategy (Wolfe et al., 2009).

Tables 3–5 provide comparative results between the isotropic and full expressions of MODIS V005 albedo using annual mean (for the absolute and relative bias) and daily mean statistics (for the absolute RMSE). The accuracy results were evaluated against coincident measurements of tower albedometer and collocated AERONET sunphotometer data at each of the study locations using 3–5 year retrieval periods. Figs. 15 and 16 show a set of bar plots that compare the mean and standard deviation of the instantaneous albedos with that of the ground measurements over a solar zenith angle range of 0–80° binned into 10-degree intervals. Results were partitioned into the VIS and NIR broadbands for the SAFARI sites (Fig. 15) and for the full SW range for all sites (Fig. 16). For these particular analyses (i.e. summary statistics, time-series plots, and scatter plots), the full inversion and backup algorithm results obtained from the MODIS BRDF/albedo product were temporally combined to reconstruct both the instantaneous and daily mean albedo retrievals.

The statistical results for the absolute bias (i.e. $\text{Tower}_{\text{mean}} - \text{MODIS}_{\text{mean}}$), relative bias (%), and absolute RMSE show some minor improvements for the full expression of actual albedo; particularly in the SW broadband. The measurement sites that were found to be less representative of the surrounding regions extending to a MODIS 500 m grid (i.e. ARM-Central Facility and NSA-Barrow) were also found to have the highest absolute RMSEs (~0.013 units of albedo larger than the other measurement sites).

The SZA dependence on the accuracy and precision of MODIS instantaneous albedos is also demonstrated in Figs. 15 and 16. In

Table 3
Comparative results between field-measured albedos and MODIS V005 albedos at the ARM-Central Facility (CF) and NSA-Barrow measurement sites using the SW (0.3–5.0 μm) broadband.

Surface albedo	NSA-Barrow (SW)	ARM-CF (SW)
Tower albedo (annual mean)	0.4367	0.2218
Sample size (# days)	305	386
$A_{\text{Isotropic}}$ (annual mean)	0.3398	0.1920
$A_{\text{Isotropic}}$ — absolute bias	−0.1305	−0.0298
$A_{\text{Isotropic}}$ — absolute RMSE	0.0578	0.0526
$A_{\text{Isotropic}}$ — relative bias	−22.19%	−13.44%
A_{Full} (annual mean)	0.3644	0.1939
A_{Full} — absolute bias	−0.0722	−0.0279
A_{Full} — absolute RMSE	0.0444	0.0518
A_{Full} — relative bias	−16.55%	−12.61%

Table 4
Comparative results between field-measured albedos and MODIS V005 albedos at the SAFARI-Mongu measurement site using the VIS (0.30–0.70 μm), NIR (0.70–5.00 μm), and SW (0.3–5.0 μm) broadbands.

Surface albedo	SAFARI-Mongu (VIS)	SAFARI-Mongu (NIR)	SAFARI-Mongu (SW)
Tower albedo (annual mean)	0.0523	0.2296	0.1623
Sample size (# days)	260	408	263
$A_{\text{Isotropic}}$ (annual mean)	0.0573	0.2489	0.1477
$A_{\text{Isotropic}}$ — absolute bias	0.0020	0.0193	−0.0146
$A_{\text{Isotropic}}$ — absolute RMSE	0.0329	0.0281	0.0395
$A_{\text{Isotropic}}$ — relative bias	9.64%	8.42%	−8.99%
A_{Full} (annual mean)	0.0543	0.2494	0.1495
A_{Full} — absolute bias	0.0050	0.0198	−0.0127
A_{Full} — absolute RMSE	0.0336	0.0286	0.0391
A_{Full} — relative bias	3.84%	8.64%	−7.84%

Table 5
Comparative results between field-measured albedos and MODIS V005 albedos at the SAFARI-Skukuza measurement site using the VIS (0.30–0.70 μm), NIR (0.70–5.00 μm), and SW (0.3–5.0 μm) broadbands.

Surface albedo	SAFARI-Skukuza (VIS)	SAFARI-Skukuza (NIR)	SAFARI-Skukuza (SW)
Tower albedo (annual mean)	0.0704	0.2252	0.1519
Sample size (# days)	622	624	621
$A_{\text{Isotropic}}$ (annual mean)	0.0681	0.2570	0.0005
$A_{\text{Isotropic}}$ — absolute bias	−0.0022	0.0317	0.0029
$A_{\text{Isotropic}}$ — absolute RMSE	0.0107	0.0422	0.0160
$A_{\text{Isotropic}}$ — relative bias	−3.14%	14.08%	0.33%
A_{Full} (annual mean)	0.0718	0.2582	0.1546
A_{Full} — absolute bias	0.0014	0.0329	0.0026
A_{Full} — absolute RMSE	0.0098	0.0431	0.0162
A_{Full} — relative bias	2.07%	14.64%	1.77%

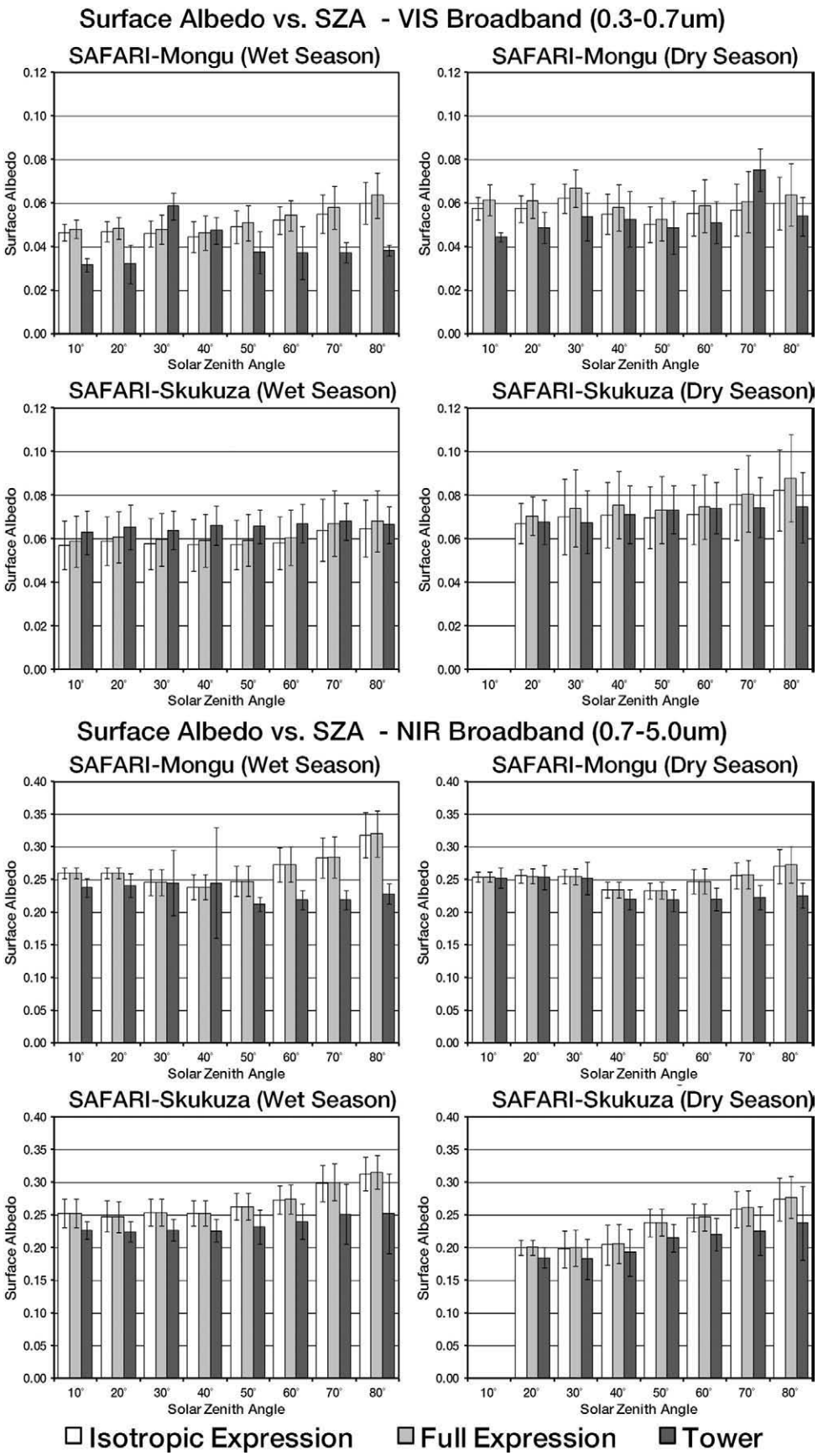

Fig. 15. Comparisons of the instantaneous albedos (both full and isotropic expressions) against ground measurements over a solar zenith angle range of 0–80° (binned into 10-degree intervals). Results were partitioned into the VIS and NIR broadbands for the SAFARI sites.

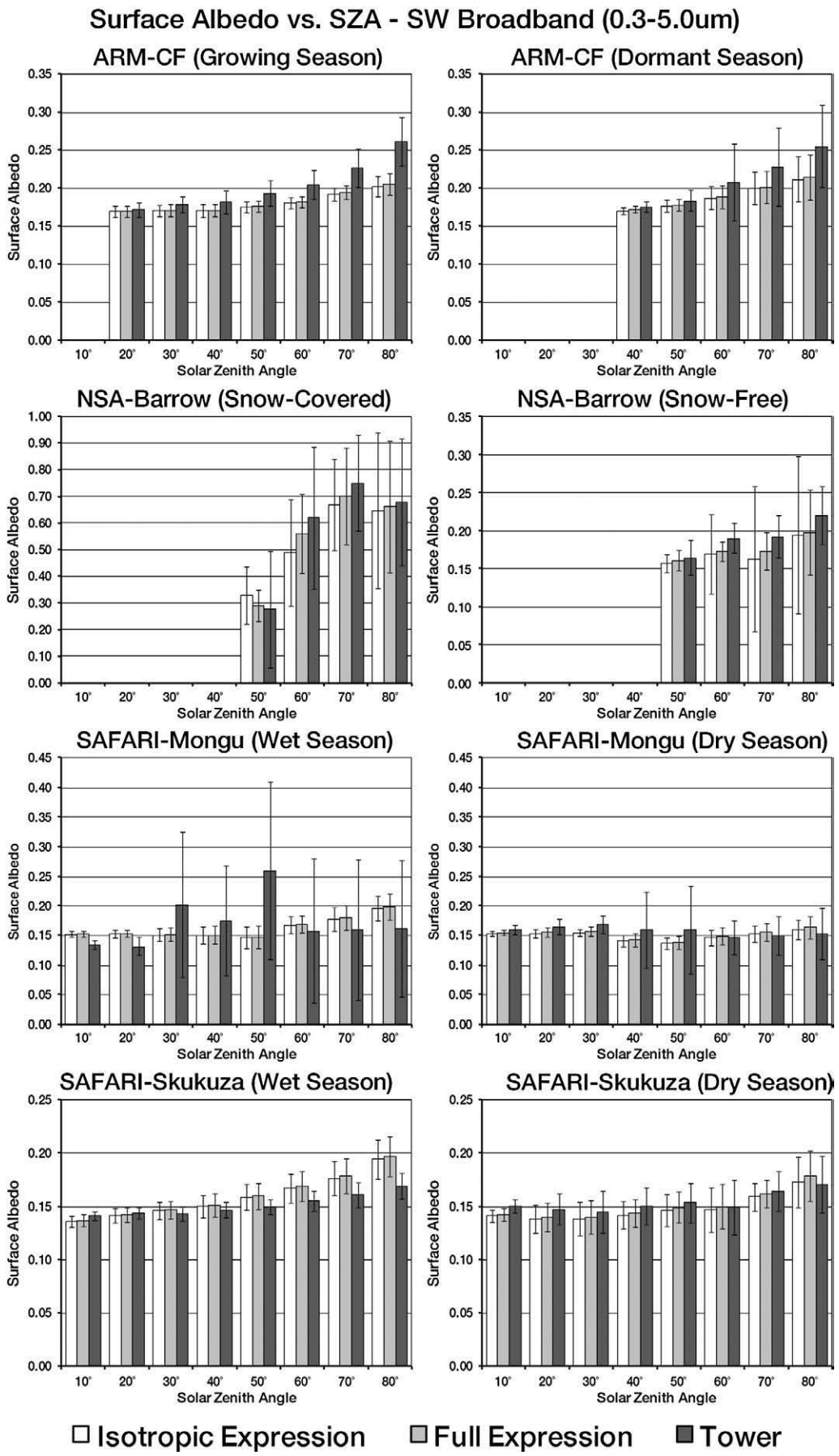

Fig. 16. Comparisons of the instantaneous albedos (for the SW broadband) against ground measurements. Setup is the same as Fig. 15.

general, the full expression of actual albedo (Eq. (60a)) increased the number of values that strongly corresponded to the ground measurements (based on both mean and standard deviation values) by 6.4%, 3.3%, and 15% (in the VIS, NIR, and SW broadbands, respectively). The isotropic expression recorded relative albedo biases within bounds of 2.1%, 0.71%, and 6.3% for SZA<50; and 6.3%, 2.2%, and 8.3% for SZA>70 (VIS, NIR, and SW broadbands, respectively). The new formulation reduced these biases to 2.0%, 0.69%, and 5.8% for SZA<50; and to 5.3%, 2.1%, and 6.9% for SZA>70 (VIS, NIR, and SW broadbands, respectively). These bounds are consistent with both the annual mean statistics (Tables 3–5) and MODTRAN simulations (in Section 5).

Results further indicate a considerable improvement in accuracy over NSA-Barrow (see Fig. 16). This occurred despite the documented uncertainties due to spatial scale (in Section 4) and the apparent lack of "full inversion" retrievals (only 28% of the 5-year observation period) over this station. Although more directional retrievals from MODIS are gained at the high latitudes, these observations are not always of the highest cloud-free quality and often occupy only a small or extreme part of the viewing and illumination hemisphere, hence causing higher retrieval uncertainties (Shuai et al., 2008). Explicit characterization of the influence of anisotropic diffuse illumination improves the instantaneous albedo retrievals from MODIS under such constrained conditions.

7. Summary

In previous studies using linear kernel-driven BRF model to calculate albedo, it is usual to consider the diffuse illumination field isotropic. As we note, this has been shown by several previous studies (and shown again here) to produce reliable results over the majority of the range of solar zenith angles. When the solar zenith exceeds around 70° and/or for optically thick atmospheres where the details of the angular variation of the diffuse illumination field may be more important, an isotropic assumption can lead to quite large errors. An additional feature missing from previous formulations of albedo using these models has been explicit consideration of the multiple scattering interactions between the atmosphere and ground that can enhance both the downwelling and the upwelling radiance.

In this paper, we present new formulations for the calculation of albedo incorporating anisotropic diffuse illumination and multiple scattering between the surface and atmosphere. For linear BRF models such as those produced by the MODIS (Collection V005) BRDF/albedo product, we have shown that albedo incorporating these features can be expressed as a slightly non-linear function of the model parameters (Eq. (60a)). The only non-linearity is a function of the proportion of diffuse illumination, the atmospheric albedo, the relative importance of the angular kernel parameters to the isotropic term and the difference between the bihemispherical integral of each kernel (*c.f.* 'white-sky albedo') and a similar integral weighted by a normalized sky radiance distribution. We denote this difference $\overline{\overline{K}}'''_{x\Lambda}$ (see Eq. (61b)). It is likely therefore that the non-linear aspect of this formulation will be rather small in most circumstances, so a linear version (Eq. (60b)) is presented. The departure of this model from albedo assuming an isotropic diffuse illumination field is controlled by the proportion of diffuse illumination and by $\overline{\overline{K}}'''_{x\Lambda}$. The larger the departure of this latter term from zero, the larger the departure of albedo from that under isotropic diffuse illumination assumptions. The way of expressing albedo developed here allows for clear insights into the mechanisms involved. What is also particularly useful about these new expressions is that should users believe they require albedo that incorporates the effects considered here, they simply need to be provided with a new set of (N_{sky}-weighted) bihemispherical integrals of the kernels. Although N_{sky} might formally be a function of atmospheric state (e.g. phrased as visibility) if the departures from zero of $\overline{\overline{K}}'''_{x\Lambda}$ are rather small in most cases, using some approximate N_{sky} such as in this study should be quite tolerant to variations in visibility. If such variations were deemed of interest, it would not be difficult to calculate $\overline{\overline{K}}'_{x\Lambda}$ for the volumetric and geometric kernels for a range of conditions from clear sky (no aerosols) through to standard overcast illumination conditions (or other more diffuse distributions). A series of simulations using the MODTRAN®5.1 radiative transfer model provided results for all the terms required to describe such effects, while maintaining the original weighted terms of the fractions of beam and diffuse skylight to estimate actual albedo.

For most study locations, the original formulation of actual albedo under conditions of isotropic illumination was improved slightly by the newly-formulated approach, with improvements in accuracy (in the daily mean albedo retrievals) ranging in 0.004–0.013 units of absolute RMSE; and improvement in the relative bias of up to 2.0%. It is most likely that when we are dealing with generally rather small improvements in albedo characterization of this sort other impacts such as errors due to scaling characterization or spectral interpolation (estimating broadband albedo from sampled narrow waveband estimates as performed here) may play increasingly important roles.

In an attempt to characterize the magnitude of the errors associated with scaling between ground measurements and satellite retrievals, semivariograms from high spatial resolution ETM+ images were examined around the tower sites. This analysis was further enhanced by examining the response of variogram model parameters at increased fields of view; thus, providing an assessment of the degree of spatial uniformity (or lack of) to determine whether the ground footprints of the tower measurements capture the intrinsic variability at the scale of MODIS observations. This spatial characterization reveals that the subpixel heterogeneity at the MODIS footprint is, in part, responsible for the discrepancies in product accuracy over the ARM-Central Facility and NSA-Barrow sites. Nonetheless, because the experimental setup focuses on coincident analyses between formulations (i.e. (1) MODIS retrievals that account for anisotropic illumination and multiple scattering; and (2) MODIS retrievals that treat the downwelling diffuse radiation as isotropic); such scaling effects did not inhibit our ability to compare the accuracies of the two approaches. Both the test cases and validation results confirm that the estimation of actual albedo under suitable conditions of isotropic illumination does not introduce relative biases of sufficient magnitude to be of concern to most users of the MODIS V005 BRDF/albedo product. Understanding which factors, and at what scales, are controlling surface albedo variability appears to be a more fundamental challenge than the latter. Furthermore, as production moves from MODIS data to NPP and NPOESS data, user specifications require that production also moves from the current multi-date approach to daily albedo computations. Thus, directional observations acquired during a single day overpass must dominate the retrieval through coupling with daily rolling surface reflectance anisotropy retrievals that provide crucial a priori knowledge of the underlying surface conditions. In particular, the directional retrievals of surface reflectance anisotropy gained at high latitudes are not always of the highest cloud-free quality and often occupy only a small or extreme part of the viewing and illumination hemisphere, hence causing higher retrieval uncertainties. The presence of snow-cover over these regions further complicates the BRDF retrieval and inversion process. This paper demonstrates that explicit characterization of the aerosol optical properties and the contribution of multiple scattering improve the instantaneous albedo retrievals from MODIS under such scenarios; thus increasing the confidence in the daily mean albedo estimates required by rigorous modeling efforts.

Acknowledgements

The authors would like to thank Dr. Alexander Berk (Spectral Sciences, Inc.), for his support in evaluating the MODTRAN®5.1-DISORT interface; and to Dr. Shunlin Liang (Department of Geography,

University of Maryland, College Park) for revising the formulation of the sky radiance. Support for this research was provided by the National Aeronautics and Space Administration (NASA) under grants NASA-NNX07AT35H and NASA-NNX08AE94A; and the U.S. Department of Energy (DOE) Atmospheric Radiation Measurement (ARM) Program under grant DOE-DE-FG02-06ER64178. This paper is dedicated in honor of the contributions of Prof. Michael Barnsley to the field of Remote Sensing of Environment through his research, publications, leadership, teaching, and mentoring of students.

References

Ackerman, T. P., & Stokes, G. (2003). The atmospheric radiation measurement program. *Physics Today*, *56*, 38−45.

Bacour, C., & Breon, F. M. (2005). Variability of biome reflectance directional signatures as seen by POLDER. *Remote Sensing of Environment*, *98*, 80−95.

Berk, A., & Anderson, G. P. (2008). Impact of MODTRAN® 5.1 on atmospheric compensation. *Geoscience and remote sensing symposium, IGARSS 2008* (pp. 127−129). Boston, MA: IEEE International.

Berk, A., Cooley, T. W., Anderson, G. P., Acharya, P. K., Bernstein, L. S., Muratov, L., et al. (2004). MODTRAN5: a reformulated atmospheric band model with auxiliary species and practical multiple scattering options, sensors, systems, and next-generation satellites. *VIII. Proceedings of the Society of Photographic Instrumentation Engineers (SPIE)* (pp. 78−85).

Buriez, J. C., Parol, F., Poussi, Z., & Viollier, M. (2007). An improved derivation of the top-of-atmosphere albedo from POLDER/ADEOS-2: 2. Broadband albedo. *Journal of Geophysical Research-Atmospheres*, *112*, D19.

Carroll, S. S., & Cressie, N. (1996). A comparison of geostatistical methodologies used to estimate snow water equivalent. *Water Resources Bulletin*, *32*, 267−278.

Chandrasekhar, S. (1960). *Radiative transfer* (pp. 1−393). New York, NY: Dover Publications, Inc.

Cosh, M. H. (2007). SGP Cloud and Land Surface Interaction Campaign (CLASIC) land surface states and fluxes experiment plan. *Atmospheric Radiation Measurement (ARM) Program*.

Davis, J. C. (1986). *Statistics and data analysis in geology*. New York: Wiley.

Gao, F., Li, X., Strahler, A. H., & Schaaf, C. (2001). Evaluation of the LiTransit kernel for BRDF modeling. *Remote Sensing Reviews*, *19*, 205−224.

Gatebe, C. K., King, M. D., Platnick, S., Arnold, G. T., Vermote, E. F., & Schmid, B. (2003). Airborne spectral measurements of surface-atmosphere anisotropy for several surfaces and ecosystems over southern Africa. *Journal of Geophysical Research*, *108*, 1−16. doi:10.1029/2002JD002397.

Grant, I., Prata, A., & Ceche, R. (2000). The impact of the diurnal variation of albedo on the remote sensing of the daily mean albedo of grassland. *Journal of Applied Meteorology*, *39*, 231−244.

Hautecoeur, O., & Leroy, M. M. (1998). Surface Bidirectional Reflectance Distribution Function observed at global scale by POLDER/ADEOS. *Geophysical Research Letters*, *25*, 4197−4200.

Henderson-Sellers, A., & Wilson, M. F. (1983). Surface albedo data for climatic modeling. *Reviews of Geophysics*, *21*, 1743−1778.

Holben, B. N., Tanre, D., Smirnov, A., Eck, T. F., Slutsker, I., Abuhassan, N., et al. (2001). An emerging ground-based aerosol climatology: Aerosol optical depth from AERONET. *Journal of Geophysical Research*, *106*, 12067−12097.

Isaaks, E. H., & Srivastava, R. M. (1989). *An introduction to applied geostatistics*. New York: Oxford University Press.

Kimes, D., Sellers, P., & Newcomb, W. (1987). Hemispherical reflectance variations of vegetation canopies and implications for global and regional energy budget studies. *Journal of Applied Meteorology*, *26*, 959−972.

King, M. D., Strange, M. G., Leone, P., & Blaine, L. R. (1986). Multiwavelength scanning radiometer for airborne measurements of scattered radiation within clouds. *Journal of Atmospheric and Oceanic Technology*, *3*, 513−522.

Lawrence, P. J., & Chase, T. N. (2007). Representing a new MODIS consistent land surface in the Community Land Model (CLM 3.0). *Journal of Geophysical Research-Biogeosciences*, *112*, G01023. doi:10.1029/2006JG000168.

Lewis, P., & Barnsley, M. (1994). Influence of the sky radiance distribution on various formulations of the Earth surface albedo. *Proceedings of the Colloque International Mesures Physiques et Signatures en Teledetection* (pp. 707−716). Val d'Isere: France.

Li, X. W., & Strahler, A. H. (1992). Geometric-optical bidirectional reflectance modeling of the discrete crown vegetation canopy — Effect of crown shape and mutual shadowing. *IEEE Transactions on Geoscience and Remote Sensing*, *30*, 276−292.

Liang, S. (2001). Narrowband to broadband conversion of land surface albedo. I. Algorithms. *Remote Sensing of Environment*, *76*, 213−238.

Liang, S. (2004). Canopy reflectance modeling. In S. Liang (Ed.), *Quantitative remote sensing of land surfaces* : John Wiley and Sons, Inc.

Liu, J., Schaaf, C. B., Strahler, A. H., Jiao, Z., Shuai, Y., Zhang, Q., et al. (2009). Validation of Moderate Resolution Imaging Spectroradiometer (MODIS) albedo retrieval algorithm: Dependence of albedo on solar zenith angle. *Journal of Geophysical Research-Atmospheres*, *114*, D01106. doi:10.1029/2008JD009969.

Lucht, W., Schaaf, C. B., & Strahler, A. H. (2000). An algorithm for the retrieval of albedo from space using semi-empirical BRDF models. *IEEE Transactions on Geoscience and Remote Sensing*, *38*, 977−998.

Lucht, W., Schaaf, C. B., Strahler, A. H., & d'Entremont, R. P. (1999). Remote sensing of albedo using the BRDF in relation to land surface properties. In M. M. Verstrate, & M. Menenti (Eds.), *Remote sensing in the context of global change issues*.

Lyapustin, A. I., & Privette, J. L. (1999). A new method of retrieving surface bidirectional reflectance from ground measurements: Atmospheric sensitivity study. *Journal of Geophysical Research*, *104*, 6257−6268.

Maignan, F., Breon, F. M., & Lacaze, R. (2004). Bidirectional reflectance of Earth targets: Evaluation of analytical models using a large set of spaceborne measurements with emphasis on the Hot Spot. *Remote Sensing of Environment*, *90*, 210−220.

Martonchik, J., Bruegge, C., & Strahler, A. H. (2000). A review of reflectance nomenclature used in remote sensing. *Remote Sensing Reviews*, *19*, 9−20.

Martonchik, J. V., Diner, D. J., Kahn, R. A., Ackerman, T. P., & Verstraete, M. M. (1998). Techniques for the retrieval of aerosol properties over land and ocean using multiangle imaging. *IEEE Transactions of Geoscience and Remote Sensing*, *36*, 1212−1227.

Materon, G. (1963). Principles of geostatistics. *Economic Geology*, *58*, 1246−1266. doi:10.2113/gsecongeo.58.8.1246.

Nicodemus, F. E. (1977). Geometrical considerations and nomenclature for reflectance. In DC Washington (Ed.), *National Bureau of Standards monograph, no. 160* (pp. 1−52).

Oleson, K. W., Bonan, G. B., Schaaf, C. B., Gao, F., Jin, Y. F., & Strahler, A. H. (2003). Assessment of global climate model land surface albedo using MODIS data. *Geophysical Research Letters*, *38*.

Pinty, B., Lattanzio, A., Martonchik, J. V., Verstraete, M. M., Gobron, N., Taberner, M., et al. (2005). Coupling diffuse sky radiation and surface albedo. *Journal of Atmospheric Sciences*, *62*, 2580−2591.

Privette, J. L., Mukelabai, M., Hanan, N., & Hao, Z. (2005). *SAFARI 2000 surface albedo and radiation fluxes at Mongu and Skukuza, 2000–2002*. Data set. Available on-line [http://daac.ornl.gov/] from. Oak Ridge, Tennessee, U.S.A: Oak Ridge National Laboratory Distributed Active Archive Center.

Rahman, H., Pinty, B., & Verstraete, M. M. (1993). Coupled surface-atmosphere reflectance (CSAR) model. 2. Semiempirical surface model usable with NOAA advanced very high resolution radiometer data. *Journal of Geophysical Research*, *98*(D11), 20,791−720,801.

Román, M. O., Schaaf, C. B., Yang, X., Woodcock, C. E., Strahler, A. H., Braswell, R. H., et al. (2009). The MODIS (Collection V005) BRDF/albedo product: Assessment of spatial representativeness over forested landscapes. *Remote Sensing of Environment*, *113*, 2476−2498. doi:10.1016/j.rse.2009.07.009.

Ross, J. (1981). *The radiation regime and architecture of plant stands*. Norwell, Mass: The Hague: Dr. W. Junk Publishers.

Roujean, J. -L., Leroy, M., Podaire, A., & Deschamps, P. Y. (1992). Evidence of surface reflectance bidirectional effects from a Noaa/Avhrr multitemporal data set. *International Journal of Remote Sensing*, *13*, 685−698.

Rutan, D. A., Rose, F. G., Smith, N. M., & Charlock, T. P. (2001). Validation data set for CERES surface and atmospheric radiation budget (SARB). *World Climate Research Programme (WCRP) Global Energy and Water Cycle Experiment (GEWEX) Newsletter* (pp. 11−12).

Salomon, J. G., Schaaf, C. B., Strahler, A. H., Gao, F., & Jin, Y. F. (2006). Validation of the MODIS Bidirectional Reflectance Distribution Function and albedo retrievals using combined observations from the Aqua and Terra platforms. *IEEE Transactions on Geoscience and Remote Sensing*, *44*, 1555−1565.

Schaaf, C. B., Gao, F., Strahler, A. H., Lucht, W., Li, X., Tsang, T., et al. (2002). First operational BRDF, albedo and nadir reflectance products from MODIS. *Remote Sensing of Environment*, *83*, 135−148.

Schaaf, C. B., Martonchik, J., Pinty, B., Govaerts, Y., Gao, F., Lattanzio, A., et al. (2008). Retrieval of surface albedo from satellite sensors. In S. Liang (Ed.), *Advances in land remote sensing: System, modeling, inversion and application* (pp. 219−243). : Springer.

Schaepman-Strub, G., Schaepman, M. E., Painter, T. H., Dangel, S., & Martonchik, J. V. (2006). Reflectance quantities in optical remote sensing-definitions and case studies. *Remote Sensing of Environment*, *103*, 27−42.

Sellers, P. J., Meeson, B. W., Hall, F. G., Asrar, G., Murphy, R. E., Schiffer, R. A., et al. (1995). Remote sensing of the land surface for studies of global change: Models & algorithms experiments. *Remote Sensing of Environment*, *15*, 3−26.

Shuai, Y., Schaaf, C. B., Strahler, A. H., Liu, J., & Jiao, Z. (2008). Quality assessment of BRDF/albedo retrievals in MODIS operational system. *Geophysical Research Letters*, *35*, L05407.

Stamnes, K. (1982). Reflection and transmission by a vertically inhomogeneous planetary atmosphere. *Planetary and Space Science*, *30*, 727−732.

Stamnes, K., Tsay, S. -C., Wiscombe, W. J., & Jayaweera, K. (1988). Numerically stable algorithm for discrete-ordinate-method radiative transfer in multiple scattering and emitting layered media. *Applied Optics*, *27*, 2502−2509.

Stamnes, K., Tsay, S. -C., Wiscombe, W. J., & Laszlo, I. (2000). DISORT, a general-purpose Fortran program for discrete-ordinate-method radiative transfer in scattering and emitting layered media: documentation of methodology. *NASA-GSFC Climate and Radiation Branch* (pp. 112). available as "DISORTReport1.1.pdf" from ftp://climate1.gsfc.nasa.gov/wiscombe/, v1.1.

Stone, R. S., Anderson, G. P., Andrews, E., Dutton, E. G., Harris, J., Shettle, E. P., et al. (2005). Asian dust signatures at Barrow: Observed and simulated. *Proceedings of the IEEE workshop on remote sensing of atmospheric aerosol, an honorary workshop for Prof. John A. Reagan* (pp. 74−79). Tucson, Arizona: University of Arizona.

Stone, R. S., Anderson, G. P., Shettle, E. P., Andrews, E., Loukachine, K., Dutton, E. G., et al. (2008). Radiative impact of boreal smoke in the Arctic: Observed and modeled. *Journal of Geophysical Research*, *113*, D14S16. doi:10.1029/2007JD009657.

Susaki, J., Yasuoka, Y., Kajiwara, K., Honda, Y., & Hara, K. (2007). Validation of MODIS albedo products of paddy fields in Japan. *IEEE Transactions on Geoscience and Remote Sensing*, *45*, 206−217.

Swap, R. J., Annegarn, H. J., & Otter, L. (2002). Southern African Regional Science Initiative (SAFARI 2000): Summary of science plan. *South African Journal of Science*, *98*, 119−124.

Wang, Z., Zeng, X., Barlage, M., Dickinson, R. E., Gao, F., & Schaaf, C. B. (2004). Using MODIS BRDF and albedo data to evaluate global model land surface albedo. *Journal of Hydrometeorology*, *5*, 3−14.

Wanner, W., Li, X., & Strahler, A. H. (1995). On the derivation of kernels for kernel-driven models of bidirectional reflectance. *Journal of Geophysical Research-Atmospheres*, *100*, 21077−21089.

Wanner, W., Strahler, A. H., Hu, B., Lewis, P., Muller, J., Li, X., et al. (1997). Global retrieval of bidirectional reflectance and albedo over land from EOS MODIS and MISR data: Theory and algorithm. *Journal of Geophysical Research*, *102*, 17143−17161.

Wolfe, R. E., Ridgway, B. L., Patt, F. S., & Masuoka, E. J. (2009). MODIS science algorithms and data systems lessons learned. In, *Proceedings of the IEEE geoscience and remote sensing symposium, IGARSS'09*. Cape Town, South Africa: IEEE International.

WWW1. SAFARI 2000 Project (2000). http://daac.ornl.gov/S2K/safari.html

WWW2. CAVE HOME PAGE (2009). http://snowdog.larc.nasa.gov/cave/

Zhanqing, L., Ackerman, T. P., Wiscombe, W. J., Stephens, G. L., & Kerr, R. A. (2003). Have clouds darkened since 1995? *Science*, *302*, 1151.

Zhou, L., Dickinson, R. E., Tian, Y., Zeng, X., Dai, Y., Yang, Z. L., et al. (2003). Comparison of seasonal and spatial variations of albedos from Moderate-Resolution Imaging Spectroradiometer (MODIS) and common land model. *Journal of Geophysical Research-Atmospheres*, *108*, 4488. doi:10.1029/2002JD003326.